The Dynamics of the East Australian Current System: The Tasman Front, the East Auckland Current, and the East Cape Current

CHARLES E. TILBURG*

Center for Ocean–Atmospheric Prediction Studies, The Florida State University, Tallahassee, Florida

HARLEY E. HURLBURT

Naval Research Laboratory, Stennis Space Center, Mississippi

JAMES J. O'BRIEN

Center for Ocean–Atmospheric Prediction Studies, The Florida State University, Tallahassee, Florida

JAY F. SHRIVER

Naval Research Laboratory, Stennis Space Center, Mississippi

(Manuscript received 10 May 2000, in final form 22 February 2001)

ABSTRACT

The dynamics of the flow field surrounding New Zealand are investigated using a series of global ocean models. The physical mechanisms governing the direction, magnitude, and location of the East Australian Current (EAC), the Tasman Front, the East Auckland Current (EAUC), and the East Cape Current (ECC) are studied using numerical simulations whose complexity is systematically increased. As new dynamics are added to each successive simulation, their direct and indirect effects on the flow field are examined. The simulations have horizontal resolutions of 1/8°, 1/16°, or 1/32° for each variable, and vertical resolutions ranging from 1.5-layer reduced gravity to 6-layer finite depth with realistic bottom topography. All simulations are forced by the Hellerman and Rosenstein monthly wind stress climatology. Analysis of these simulations shows that several factors play a critical role in governing the behavior of the examined currents. These factors include 1) mass balance of water pathways through the region, 2) gradients in the wind stress curl, 3) nonlinear flow instabilities, and 4) upper-ocean–topographic coupling due to mixed baroclinic and barotropic instabilities. Transport streamfunctions of a linear reduced gravity model reproduce the large-scale features well but produce an EAUC that flows counter to the observed direction. The residual of the mass balance of the transport through the Tasman Sea, the basinwide transport at 32°S, and the transport of the South Pacific subtropical gyre east of New Zealand determines the direction of the EAUC. The 6-layer nonlinear model allows isopycnal outcropping, which changes the transport through the Tasman Sea and produces an EAUC flowing in the observed direction. Gradients in the zonally integrated wind stress curl field determine the coastal separation points of the EAC, the EAUC, and the ECC, while a combination of nonlinear flow instabilities and upper-ocean–topographic coupling contribute to the formation of meanders in the Tasman Front. Increased resolution results in greater mixed baroclinic–barotropic instabilities and thus more upper-ocean–topographic coupling and surface variability, giving a more accurate simulation of topographically controlled mean meanders in the Tasman Front.

1. Introduction

The East Australian Current is the western boundary current of the South Pacific subtropical gyre. The partial separation of this current from the coast of Australia and its subsequent eastward flow into the South Pacific creates one of the most complicated and dynamically interesting regions in the world's oceans (Godfrey et al. 1980). Extending from the Coral Sea to the Tasman Sea, the East Australian Current (EAC) system generates numerous eddies and has several branches including the Tasman Front, the East Auckland Current (EAUC), the East Cape Current (ECC), and the EAC extension. A schematic of the flow field (Fig. 1) reveals a boundary current system that affects the flow along much of the eastern coasts of Australia and New Zealand. The region is highly variable due to eddy generation and extensive

* Current affiliation: Graduate College of Marine Studies, University of Delaware, Newark, Delaware.

Corresponding author address: Dr. Charles E. Tilburg, Graduate College of Marine Studies, University of Delaware, 102 Robinson Hall, Newark, DE 19716.

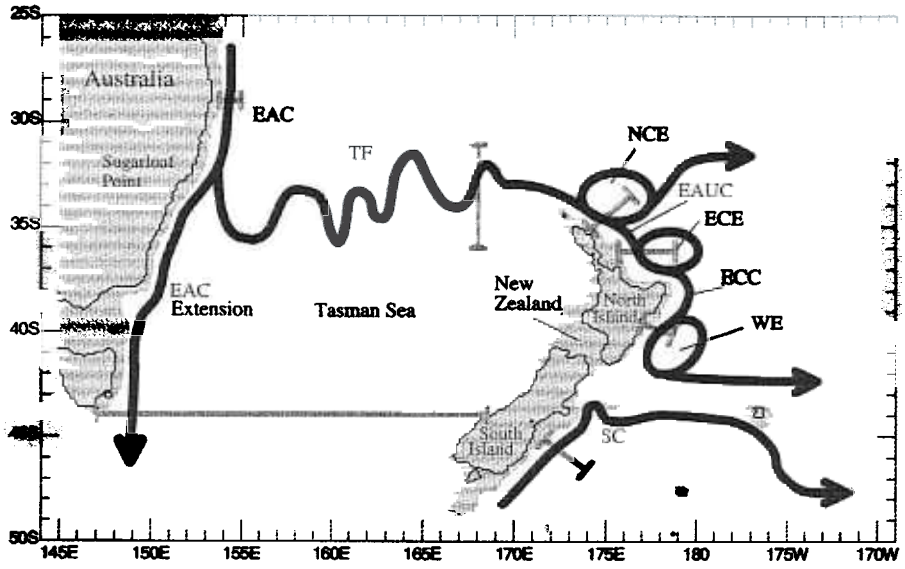

FIG. 1. Schematic diagram of the major surface currents, features and transport sections (gray lines) in the Tasman Sea, and the region surrounding New Zealand. EAC = East Australian Current, EAUC = East Auckland Current, ECC = East Cape Current, TF = Tasman Front, SC = Southland Current, NCE = North Cape Eddy, ECE = East Cape Eddy, WE = Wairarapa Eddy.

current meandering. Bottom steering significantly affects the surface flow, and a large part of the complexity of the region can be attributed to the varied bottom topography (Fig. 2), which is dominated by the extensive New Zealand submarine platform.

Unlike other western boundary currents, such as the Kuroshio and the Gulf Stream, the strength of the EAC varies substantially with time. The mass transport within eddies spawned by the EAC can be much larger than its mean flow (Ridgway and Godfrey 1997; Lilley et al. 1986). Composites of ship and satellite observations show that a large portion of the EAC leaves the coast of Australia between 30° and 34°S, while a weaker flow continues southward attached to the coast. Godfrey et al. (1980) demonstrated that, although the exact separation point varies seasonally, the mean behavior of the EAC flow field is significantly different on either side of a line extending south-southeast of Sugarloaf Point (32.5°S). Just south of Sugarloaf Point, northward shelf currents are common and eddies are essentially circular, while just north of this point the currents are southward and eddies are much more elongated. Although the majority of the EAC separates from the Australian coast and either proceeds eastward or recirculates, as much as 1/3 of the original EAC exits the southern edge of the Tasman Sea, trapped against the western boundary (Ridgway and Godfrey 1997; Chiswell et al. 1997).

As the separated portion of the EAC proceeds eastward toward New Zealand, it crosses the northern edge of the Tasman Sea following a narrow, meandering pathway. Warren (1970) first suggested that this flow, associated with the Tasman Front, is a zonal jet connecting the EAC with the western boundary currents on the eastern coast of New Zealand. Stanton (1976) first identified a variable frontal jet near the Norfolk Ridge between 165° and 169°E. Denham and Crook (1976) showed that the Tasman Front extends from the Norfolk Ridge to the Lord Howe Rise (~160°E). An oceanographic survey detailed by Andrews et al. (1980) described a front that exists along the entire northern edge of the Tasman Sea. Other investigations of the meanders and variability of this front (Stanton 1979, 1981; Mulhearn 1987) at different locations demonstrated that, although the Tasman Front is highly variable, its mean path follows meanders that are permanent features of the flow field. The most probable path (shown as a white line in Fig. 2) was constructed by combining a similar diagram by Mulhearn (1987) and a mean frontal path obtained from a number of cruises described by Stanton (1979). Mulhearn (1987) used a series of satellite infrared images to determine the most probable path of the Tasman Front from 153° to 164°E during 29 months from March 1982 to April 1985. Stanton (1979) showed the location of the Tasman Front between 166° and 170°E for five different cruises from 1966 to 1975. Combining these observations reveals a most probable path of the Tasman Front that leaves the coast of Australia at 33°S, 153°E and meanders eastward between latitudes of 36° and 32°S. Although the front shows substantial variability, the mean path includes several permanent meanders.

Heath (1985a) provided a thorough summary of the flow field surrounding New Zealand. Once the eastward flow along the Tasman Front reaches the northernmost point of New Zealand, it turns southeastward, becoming the EAUC and following the northeast coastline of New

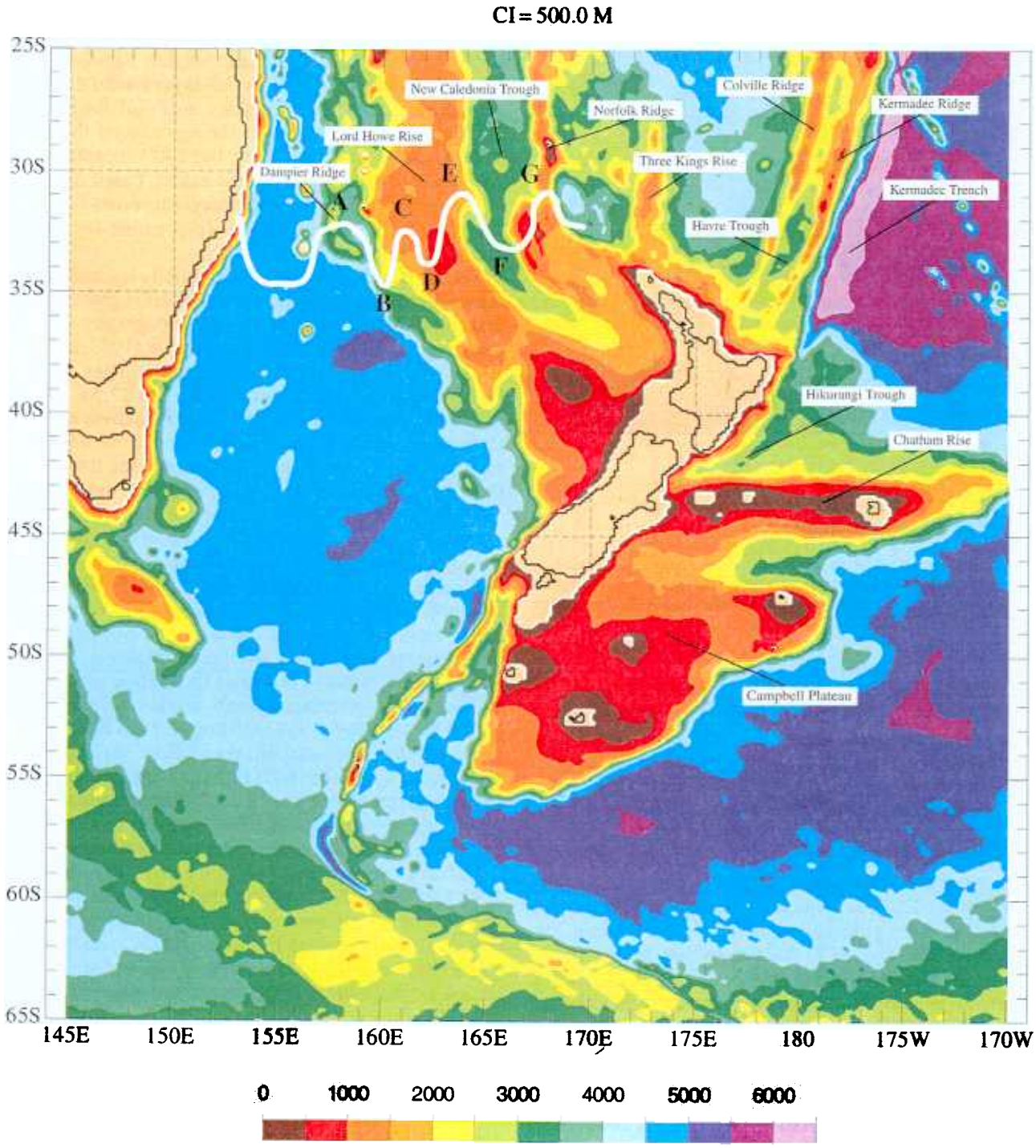

FIG. 2. Seafloor topography surrounding New Zealand. Note the large New Zealand submarine platform and the extensive ridges and troughs throughout the area. The white line represents the most probable path of the Tasman Front adapted from a similar figure by Mulhearn (1987) and a compilation of observations by Stanton (1979). The letters associated with the meanders are used to distinguish each meander for discussion in later sections.

Zealand's North Island. Although the majority of the flow gradually separates from the coast and continues eastward, a small portion remains attached to the coast and continues to the easternmost tip of North Island, East Cape. As the flow rounds East Cape, it becomes the ECC. The ECC separates from North Island at approximately 42°S and proceeds eastward slightly north of the Chatham Rise (Heath 1985a,b).

Although pathways of the EAUC and the ECC are highly variable (Laing et al. 1996), a mean dynamic

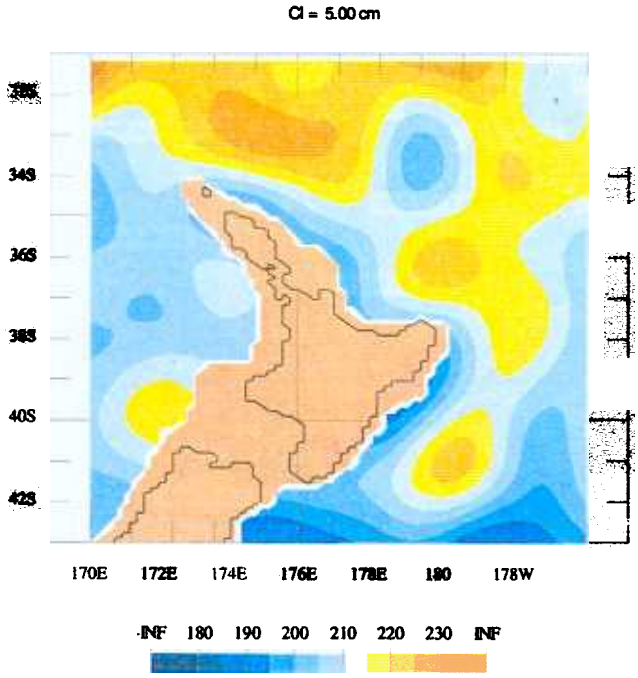

FIG. 3. Climatological dynamic sea surface height (dynamic cm) with respect to 2000 db in the region north of New Zealand compiled by Roemmich and Sutton (1998). Note the presence of the three eddies labeled in Fig. 1: NCE, ECE, and WE.

height field (Fig. 3) presented by Roemmich and Sutton (1998) shows that three quasi-stationary eddies are present in the flow field. The North Cape Eddy (NCE), the southern edge of which is the beginning of the EAUC, is centered near 33°S, 173.5°E. The East Cape Eddy (ECE), the southern edge of which comprises the end of the EAUC and the beginning of the ECC, is centered near 35.5°S, 178.5°E. The Wairarapa Eddy (WE), the western and southern edges of which compose the majority of the ECC, is centered near 41°S, 178.5°E. Also present in the dynamic height field is a relative low between NCE and ECE. Uddstrom and Oien (1999), using satellite derived sea surface temperatures (SST), were also able to identify the NCE and the WE, although they did not find a robust ECE.

Although there have been relatively few numerical simulations of this region, both linear and nonlinear models have been used to study its dynamics. Godfrey (1973) presented a qualitative study of the EAC using results derived from a regional Bryan and Cox (1968) model, an idealized flat-bottom six-level nonlinear simulation using annual wind stress and differential heating. He found that the simulated eddies and fluctuations were similar to observations, but that the model was unable to reproduce the observed vorticity balance or seasonality of the EAC due to its lack of bottom topography and use of annual wind stress climatology. Bye et al. (1979), using a diagnostic linear regional model driven by specified density, wind stress, and flow boundaries, obtained a steady-state flow field around New Zealand, reproducing the EAUC, the ECC, and the Southland Current but were unable to resolve the quasi-stationary eddies surrounding New Zealand. De Szoeke (1987) used a linear reduced gravity 3.5-layer model driven by annual wind stress encompassing the South Pacific from 57°S to almost the equator. He reproduced the large-scale features well, including the EAC separation and basinwide density surfaces. His model, based on that of Luyten et al. (1983), did not incorporate cross-isopycnal flux, which he suspected was responsible for weaker than observed shallow currents.

Semtner and Chervin (1992) briefly examined this region in the context of their ½° 20-level global model that incorporated realistic bottom topography and was driven by the Hellerman and Rosenstein (1983, hereafter HR) monthly wind stress climatology. They found a highly variable EAC ranging from 7 to 47 Sv (10^6 m^3 s^{-1}) flowing southward and a highly baroclinic transport through the Tasman Sea, ranging from 3 Sv northward to 10 Sv southward. The simulated surface flow within the Tasman Sea was northward, while the deeper levels were southward. Examination of the surface flow field reveals the presence of the three observed eddies surrounding New Zealand, meanders in the Tasman Front, and currents surrounding New Zealand flowing in the observed direction. Closer investigation, however, shows that the simulated meanders do not agree with observations in terms of amplitude or phase. Ridgway and Godfrey (1994) compared their observations to a simple linear Sverdrup–Munk model of the World Ocean by Godfrey (1989), finding that the linear model produced the observed patterns of EAC separation and transport through the Tasman Sea. They noted that the southward transport through the Tasman Sea was higher than observed and that the linear model was unable to reproduce the eddies or meanders of the observed flow.

In this paper, we build on this earlier work by using 1/8°, 1/16° and 1/32° multilayered global ocean models to examine the dynamics governing the flow field encompassing the Tasman Front, the EAUC, and the ECC. The EAC and the flow around New Zealand are situated in one of the most diverse and interconnected regions of the world's oceans, influenced by the Antarctic Circumpolar Current (ACC), the Indo–Pacific Throughflow (IPT), and the global thermohaline circulation. A global model is necessary to capture the range of essential dynamics. Increasingly realistic and dynamically complex simulations are performed to determine which dynamics are most important in governing the different aspects of the flow field. The ocean model and numerical simulations used in this investigation are discussed in section 2. The results and dynamical interpretation of the different simulations are discussed in section 3, while summary and conclusions are given in section 4.

2. The ocean model

The numerical model used in these investigations is the Naval Research Laboratory Layered Ocean Model

(NLOM), a primitive equation layered formulation with equations that have been integrated through each layer. This model is a descendent of the model detailed by Hurlburt and Thompson (1980) with greatly expanded capabilities (Wallcraft 1991; Wallcraft and Moore 1997; Moore and Wallcraft 1998). The equations for the n-layer finite-depth, hydrodynamic model are given below for layers $k = 1, \cdots, n$ with $k = 1$ for the top layer. In places where k is used to index model interfaces, $k = 0$ is the surface and $k = n$ is the bottom:

$$\frac{\partial U_k}{\partial t} + \frac{1}{a\cos\theta}\left[\frac{\partial(U_k u_k)}{\partial\phi} + \frac{\partial(V_k u_k \cos\theta)}{\partial\theta} - V_k(u_k \sin\theta + a\Omega \sin 2\theta)\right]$$
$$= \max(0, -\omega_{k-1})u_{k-} + \max(0, \omega_k)u_{k+1} - [\max(0, -\omega_k) + \max(0, \omega_{k-1})]u_k$$
$$+ \max(0, -C_M\omega_{k-1})(u_{k-1} - u_k) + \max(0, C_M\omega_k)(u_{k+1} - u_k) - \frac{h_k}{a\cos\theta}\sum_{j=1}^{n} G_{kj}\frac{\partial(h_j - H_j)}{\partial\phi}$$
$$+ (\tau_{\phi_{k-1}} - \tau_{\phi_k})/\rho_o + \frac{A}{a^2\cos^2\theta}\left[\frac{\partial(h_k e_{\phi\phi_k}\cos\theta}{\partial\phi} \quad \frac{\partial(h_k e_{\phi\theta_k}\cos^2\theta}{\partial\theta}\right] \tag{1}$$

$$\frac{\partial V_k}{\partial t} + \frac{1}{a\cos\theta}\left[\frac{\partial(U_k v_k)}{\partial\phi} + \frac{\partial(V_k v_k \cos\theta)}{\partial\theta} + U_k(u_k \sin\theta + a\Omega \sin 2\theta)\right]$$
$$= \max(0, -\omega_{k-1})v_k + \max(0, \omega_k)v_{k+1} - [\max(0, -\omega_k) + \max(0, \omega_{k-1})]v_k$$
$$+ \max(0, -C_M\omega_{k-1})(v_{k-1} - v_k) + \max(0, C_M\omega_k)(v_{k+1} - v_k) - \frac{h_k}{a}\sum_{j=1}^{n} G_{kj}\frac{\partial(h_j - H_j)}{\partial\theta}$$
$$+ (\tau_{\theta_{k-1}} - \tau_{\theta_k})/\rho_o + \frac{A}{a^2\cos^2\theta}\left[\frac{\partial(h_k e_{\phi\theta_k}\cos\theta}{\partial\phi} + \frac{\partial(h_k e_{\theta\theta_k}\cos^2\theta}{\partial\theta}\right] \tag{2}$$

$$\frac{\partial h_k}{\partial t} + \nabla\cdot\mathbf{V}_k = \omega_k - \omega_{k-} \tag{3}$$

Notation that is common in oceanography is used in the model equations. A full explanation of the parameters and notation used in these equations is given in the appendix. The model boundary conditions are kinematic and no slip. The model equations are integrated on a C grid (Mesinger and Arakawa 1976) using a semi-implicit numerical scheme for the finite-depth simulations and an explicit numerical scheme for reduced-gravity simulations.

Although thermodynamic versions of the model exist (Metzger et al. 1992; Heburn 1994; Metzger and Hurlburt 1996), the versions used in this investigation are hydrodynamic with constant density in each layer. As a result, thermal forcing and steric anomalies due to seasonal heating and cooling are excluded. The model does permit isopycnal outcropping via ventilation of model layer interfaces. This ventilation is achieved by a process known as "hydromixing" (Wallcraft 1991). When any layer's thickness decreases to a certain minimum value (h_k^+), water is entrained from the layer below at a velocity (ω_k) needed to prevent negative layer thickness. Mass and volume are conserved within each layer by compensating domainwide diapycnal mixing. The pattern of vertical mixing is determined by isopycnal outcropping and observed oxygen saturation values as discussed in detail by Shriver and Hurlburt (1997). Isopycnal outcropping and vertical mixing permit overturning circulations in the vertical, such as the thermohaline circulation and meridional overturning, and allow shallow layers on basinwide scales. Isopycnal outcropping and vertical mixing can also affect horizontal mass transports, which is an especially important mechanism in our region of interest, as will be seen in section 3b.

A modified version of the 1/12° ETOPO5 bottom topography (National Oceanic and Atmospheric Administration 1986) is used in the simulations requiring realistic bottom topography. The topography is first interpolated to the model grid and then smoothed twice with a nine-point smoother to reduce energy generation at smaller scales that are poorly resolved by the model. The maximum depth of the model is set at 6500 m. The minimum depth, set at 200 m, is used as the model boundary with a few exceptions where shallower depths are needed to connect semienclosed seas. The bottom topography is confined to the lowest layer (Hurlburt and Thompson 1980) to prevent numerical difficulties arising when moving layer interfaces intersect with sloping topography and to greatly decrease the computer time/model year. Two of the main reasons for including bot-

TABLE 1. Shown are World Ocean simulations, where, in cases using realistic bottom topography, a scaling factor was used to restrict bottom topography features to layer 6. The model is run in linear mode by scaling the winds down by a factor of 1000. The model fields are then scaled up by a factor of 1000 to restore them to their proper magnitude.

Experiment	A ($m^2 s^{-1}$)	H (m)	Model years spanned	Comments
		250/∞	250–325	Linear
		250/∞	325–450	Linear, removed New Zealand
		250/∞	325–518	Linear, friction patch in Tasman Sea
		250/∞	325–578	Linear, Indo–Pacific Throughflow closed
		155/185/210/225/225/5500	282–299	Nonlinear, flat bottom
		155/185/210/225/225/∞	389–412	Nonlinear, reduced gravity
		155/185/260/375/525/variable	860–975	Nonlinear, realistic bottom topography
		155/185/260/375/525/variable	847–899	Nonlinear, realistic bottom topography
		155/185/260/375/525/variable	910–917	Nonlinear, realistic bottom topography

tom topography, regulating baroclinic instabilities and forcing abyssal flow to follow f/h contours, are relatively unaffected by this modification of the bottom topography.

The simulations used in this investigation are defined in Table 1, and the model parameters are given in Tables 1 and 2. The density for each layer was obtained from the Levitus (1982) ocean climatology. In the 6-layer simulations, the depths of the two upper layers were chosen to represent a surface layer and a layer containing the equatorial undercurrent, while the mean fifth interface depth was chosen to represent the boundary between intermediate and abyssal water. The simulations were forced by the HR monthly wind stress climatology to statistical equilibration and were initialized from equilibrated lower-resolution simulations. All means shown are calculated from the last four years of the simulation. Numerous model-data comparisons have been performed using 1/8°–1/64° simulations from Atlantic versions of this model (Hurlburt and Hogan 2000) and different 1/8° and 1/16° simulations from a Pacific version of the model (e.g., Mitchum 1995; Hurlburt et al. 1996; Mitchell et al. 1996; and Metzger and Hurlburt 1996). Other studies have used variations of the global model to investigate the effect of the IPT on the global thermohaline circulation (Shriver and Hurlburt 1997) and the role of Halmahera Island in the transport pathways of Pacific waters to the Indian Ocean (Morey et al. 1999).

3. Climatological dynamics

We rely on the modularity of NLOM, progressing from a simple linear reduced-gravity 1/8° model to highly realistic 1/16° 6-layer simulations incorporating nonlinear dynamics and realistic bottom topography to de-

TABLE 2. Shown are additional parameters, where the numbers 1–9 in the simulations column refer to the simulations as follows: 1, RG1; 2, RG2; 3, RG3; 4, RG4; 5, FB; 6, RG5.5; 7, RB8; 8, RB16; 9, RB32. A model parameter that is not applicable for that simulation is indicated by N/A.

Parameters	Value	Simulations	Definition
C_b	0		Bottom drag coefficient
	2×10^{-3}		
	N/A		Value that topographic amplitude with respect to 6500 m was multiplied by
	0		
	0.65		
	0.69		
C_k	0		kth interfacial stress coefficient
g	9.8 m s^{-2}		Acceleration due to gravity
h_k^+	N/A		Thickness of layer k at which entrainment starts
	50/40/40/40/40 m		
σ_k	25.45/27.55		Density of layer k
	25.24/26.47/26.99/27.23/27.39/27.77		
	25.25/26.59/27.03/27.30/27.53/27.77		
$\Delta\theta$	1/8°		Latitudinal grid resolution
	1/16°		
	1/32°		
$\Delta\phi$	45/256°		Longitudinal grid resolution
	45/512°		
	45/1024°		
	N/A		kth interface vertical reference mixing velocity
	0.02 m s^{-1}		
	0.04 m s^{-1}		
	0.05/0.06/0.05/0.05/0.05 m s^{-1}	8, 9	

termine which dynamics govern specific behavior in the flow field. In addition, a 1/32° simulation is used to investigate simulation convergence with increased resolution. As the simulations increase in complexity, they more closely reproduce the observed features, suggesting that the new dynamics introduced with the new simulation are responsible for the observed features. The inherent nonlinearity of ocean dynamics complicates this analysis process, since the flow field resulting from the addition of a new physical mechanism may be due directly to the new addition or to its interaction with other dynamics. However, the relative roles of separate physical mechanisms can be investigated by diagnostic calculations and careful comparison of simulations involving different dynamics. Qualitative and quantitative model-data comparisons are made throughout this discussion to determine how well each successive simulation reproduces the observed flow field.

a. *Linear dynamics*

The lowest-order estimate of the dynamics governing the flow around New Zealand is a linear model (labeled RG1, Table 1), the dynamics of which are essentially those of a Sverdrup (1947) interior with Munk (1950) western boundary layers and globally applied horizontal friction. The flow and sea surface height are calculated using a global numerical model with realistic coastline geometry and monthly climatological wind forcing. The model has one vertical mode and a bottom layer that is infinitely deep and at rest. Since the linear simulation reveals the lowest-order response to external forcing, it can be used as a baseline for the more complicated simulations that incorporate nonlinearities, bottom topography, multiple vertical modes, flow instabilities, and isopycnal outcropping.

The mean transport streamfunctions of the 1.5-layer linear 1/8° reduced-gravity simulation driven by the HR monthly wind stress climatology (Fig. 4a) reveal a system of nested anticyclonic gyres encompassing the Southern Hemisphere. Nested gyres were also identified numerically by De Szoeke (1987) and Godfrey (1989) and observationally by Davis (1998), using neutral buoyancy floats. A large supergyre extends through all three oceans following two different paths connecting the Pacific and Indian Oceans: one path extends through the IPT (purple, dark blue, and blue contours), while the other travels south of Australia (light blue and blue-green contours). Two smaller gyres compose an inner nesting: one gyre occupies the South Atlantic and Indian Oceans (dark green to maroon contours) and the other occupies the South Pacific Ocean and extends south of Australia (dark green contour bounded on west by Australia). Three gyres, one bounded on the west by Australia (yellow, orange, and red contours), the other two bounded by New Zealand (light green contours), compose the innermost nesting in our region of interest. Closer inspection of the region east of Australia (Fig. 4b) reveals how the currents of interest are connected to the larger flow field. The EAC and ECC are western boundary currents of the innermost nested gyres. The Tasman Front is the southern edge of the innermost gyre bounded by Australia. The northern anticyclonic gyre east of New Zealand is bounded on the west by the ECC, but the southern one is unobserved. The southward western boundary current associated with this gyre disagrees with the observed northward Southland Current and its subsequent eastward flow at the Chatham Rise as described by Chiswell (1996), Stramma et al. (1995), and Uddstrom and Oien (1999). Likewise, the simulated EAUC, the western boundary current connecting the two northern inner gyres, flows opposite to the observed direction (northwestward in the linear simulation versus southeastward observed). The simulated EAC and ECC both separate from the western boundaries at the observed locations (centered near 32°S on the east coast of Australia and near 42°S on the east coast of New Zealand, respectively), while the simulated Tasman Front appears in the correct geographic location.

Although observational values of the transports are sparse, a rudimentary model-data comparison can be made. The simulated linear EAC is 25.9 Sv, which agrees well with observational values. Ridgway and Godfrey (1997) estimated the flow of the EAC relative to 2000 db, using steric heights derived from historical hydrology and expendable bathythermograph (XBT) data collected in the region, and found that the EAC varies between 27.4 and 36.3 Sv seasonally. Chiswell et al. (1997), using CTD data gathered over five cruises between 1990 and 1994, estimated the geostrophic transport of the EAC relative to 2000 db to be between 22.2 and 42.2 Sv. The simulated linear transport associated with the Tasman Front, 10.6 Sv, also agrees well with observational values. Stanton (1979), using bathythermograph (BT) data, calculated geostrophic volume transport relative to 1000 db to be 7.6–8.5 Sv, which was slightly lower than his previous observations of 9–12 Sv (Stanton 1976). Andrews et al. (1980), using XBT data, estimated the net zonal transport to be approximately 15 Sv relative to 1300 db. More recent observations yielded integrated volume transports measured at 173°E ranging from −7.1 to 16.5 Sv over a 4-yr time frame (Chiswell et al. 1997). However, the authors hypothesized that the negative transport value in the Tasman Front transport was due to an error in measurement and should not be considered evidence of a westward flow into the Tasman Sea (Chiswell et al. 1997). The simulated transports from RG1 for selected sections along with those from the subsequent simulations and observations are summarized in Table 3. The transport sections surrounding New Zealand are shown as gray lines in Fig. 1.

As noted, there are some discrepancies between the linear simulation and observations. The simulated linear EAUC (3.1 Sv to the west-northwest) is opposite in direction to observations, which show part of the flow

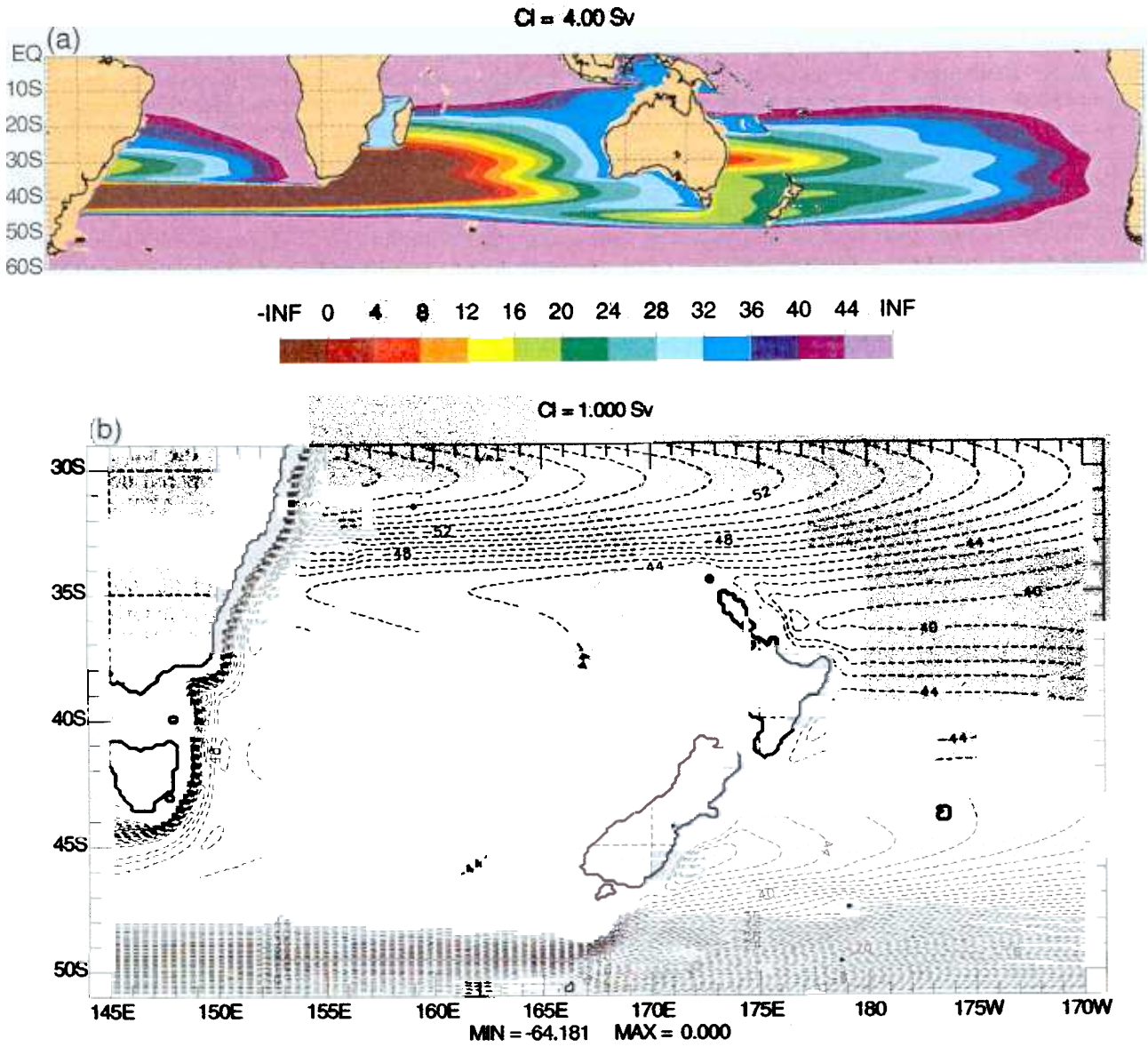

FIG. 4. (a) Mean transport streamfunctions from the 1/8° linear 1.5-layer simulation RG1 for the Southern Hemisphere depicting the interbasin supergyre and the nested intrabasin gyres. The contour interval is 7.5 Sv (10^6 m^3 s^{-1}). The modeled land boundaries are chosen to be the 200-m isobath and are shown in all figures with the actual land superimposed over the modeled land. Flow proceeds with higher valued streamfunction to the right. Note the locations of the EAC, EAUC, ECC, and Tasman Front. The EAC and ECC separation points agree with observations. The contours are colored to allow identification of different gyres. (b) Close-up of the mean transport streamfunctions from the 1/8° linear 1.5-layer global simulation RG1 for the region surrounding New Zealand. Note the incorrect direction of the EAUC.

along the Tasman Front continuing along the northeast coast of New Zealand. Heath (1985b) describes an east-southeast flow of 2–10 Sv, while other observations (Stanton et al. 1997) describe larger transports of 11–34 Sv. The simulated ECC (2.1 Sv southward) is much less than the observed 22 Sv (Stanton et al. 1997). The simulated net southward transport through the Tasman Sea (12.1 Sv) is higher than observed values of 7.1 Sv at 44°S (Ridgway and Godfrey 1997) and 6.3–9.2 Sv at 43°S (Chiswell et al. 1997). Also, the southward-flowing boundary current along South Island disagrees with the observed northward-flowing Southland Current. These discrepancies suggest that linear dynamics are unable to explain some aspects of the flow field, and more complicated processes are necessary to fully describe this region.

Since the linear model agrees with observed locations of EAC separation, we are able to use linear theory to investigate the baseline dynamics behind this phenomenon. The unique position of New Zealand (directly in the path of a separating western boundary current) has fueled speculation concerning the role of the island in the separation of the EAC. Two main theories concerning its role focus on two different aspects of the flow.

TABLE 3. Shown is mean transport from selected sections, where values are given in Sverdrups (10^6 m^3 s^{-1}). Negative means west or south. Positive means east or north. All simulated transports are for the top five layers, corresponding to the simulated thermocline. These transport sections are shown in Fig. 1 as gray lines.

Experiment	Pacific Ocean[a] at 32°S	Pacific Ocean[b] at 39°S	Tasman Sea[c]	East Australian Current[d]	Tasman Front[e]	EAUC (after separation)[f]	EAUC (before separation)[g]	East Cape Current[h]
RG1	**16.5**	**25.5**	−12.1	−25.9	10.6	3.1	−2.5	−2.1
RG2	**16.5**	**28.4**	−11.9	−25.9	13.4	—	—	—
RG3	**16.8**	**25.3**	−7.6	−25.5	14.6	−0.9	−6.5	−6.5
RG4	**0.0**	**25.5**	−28.7	−42.4	10.5	3.2	−2.4	−2.1
FB	**11.7**	**21.1**	5.3	−26.7	31.6	−13.5	−24.6	−14.9
RB8	**13.6**	**17.1**	0.1	−27.2	23.1	−3.8	−31.0	−11.7
RB16	**12.2**	**14.1**	6.4	−28.0	27.5	−8.5	−36.8	−15.9
Observations[i]	**5–26**		−6.3 to −9.2	−22.2 to − 42.2	7.6–16.5	−2 to −11	−10 to −34	−22

[a] This transport corresponds to the basinwide equatorward movement out of our region of interest. Since the model excludes transport through the Bering Sea, this value can be used as a proxy for the IPT and be compared to observations of the IPT to validate the model.
[b] This transport corresponds to the equatorward movement of the south Pacific subtropical gyre. For mass balance, Pacific Ocean across 32°S + Tasman Sea + Pacific Ocean across 39°S + EAUC (after separation) must equal the vertical mixing between layers 5 and 6 (which is very small).
[c] Transport through the Tasman Sea at 44°S.
[d] Meridional transport between the coast of Australia and 154.8°E at 29°S.
[e] Zonal transport between 31° and 36°S at 168.2°E.
[f] Alongshore transport between coast and 36.0°S, 178.9°E. Positive corresponds to northwestward; negative corresponds to southeastward.
[g] Alongshore transport between coast and 33.6°S, 176.5°E. Positive corresponds to northwestward; negative corresponds to southeastward.
[h] Alongshore transport between coast and 40.0°S, 178.6°E. Positive corresponds to northward; negative corresponds to southward.
[i] Observations from all studies mentioned in the text. Note that the *observed* transports at 32°S are actually observations of IPT transport.

The first states that New Zealand blocks the westward-propagating Rossby waves south of 34°S, causing the EAC to separate at this latitude instead of much farther south (Warren 1970). The second states that the coastline geometry of Australia (i.e., the bend in the coastline at Sugarloaf Point) causes the separation (Godfrey et al. 1980; Ou and De Ruijter 1986), and the presence of New Zealand is unimportant.

Transport streamfunctions from a simulation (Fig. 5) where New Zealand has been removed (RG2) demonstrate that the removal of New Zealand does not alter the separation latitude of the EAC. In a linear simula-

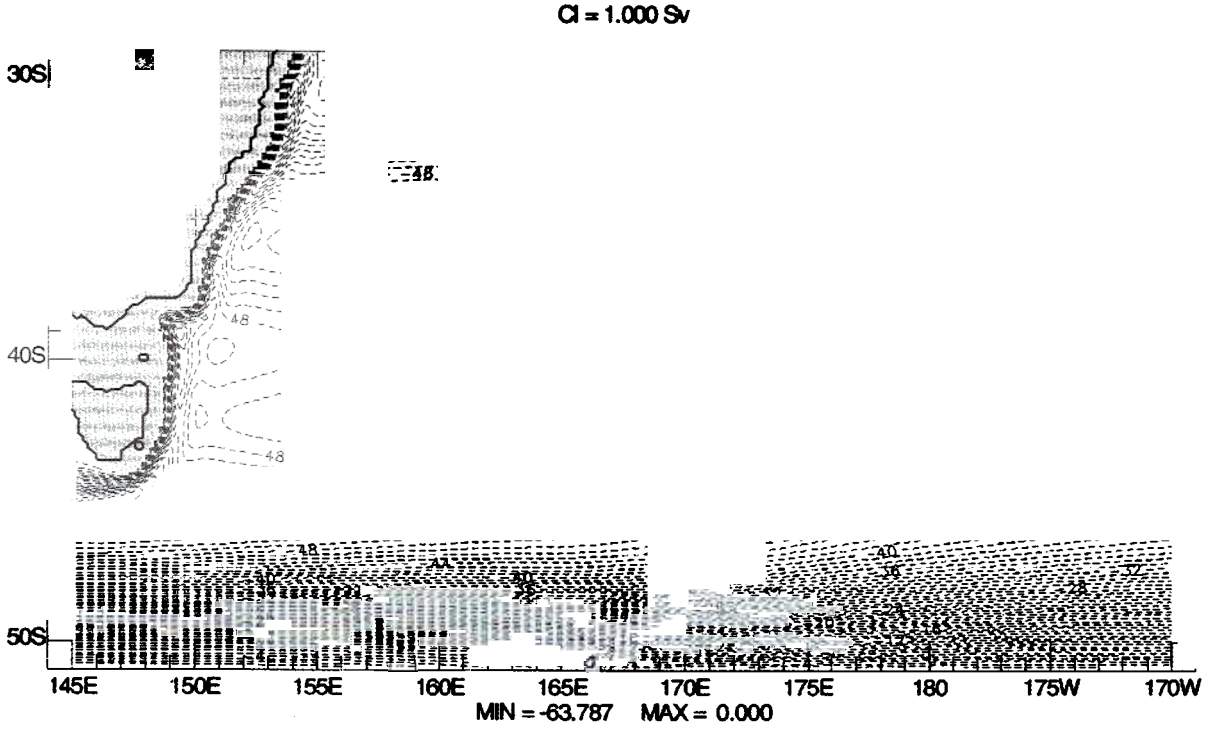

FIG. 5. Mean transport streamfunctions from the 1/8° linear 1.5-layer global simulation RG2 with New Zealand removed from the flow field. Note that the EAC separation point is still between 30° and 34°S, in agreement with observations and RG1.

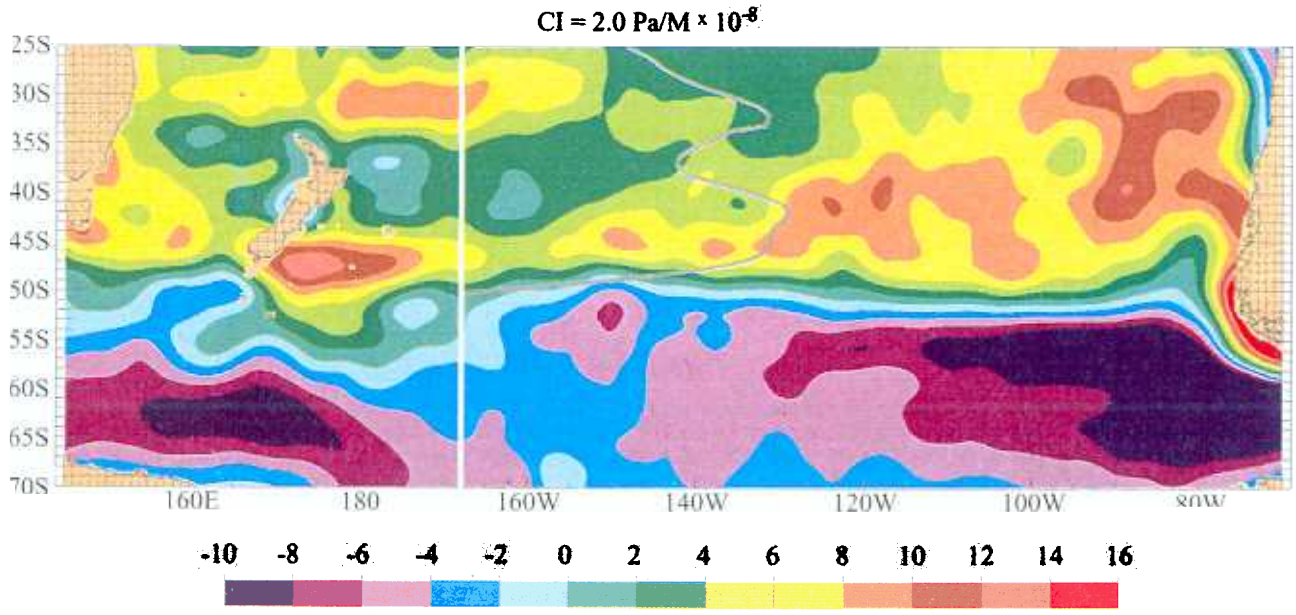

FIG. 6. Annual mean wind stress curl field derived from Hellerman and Rosenstein (1983). Note the large negative curl in the Antarctic region. The gray line represents the zonal wind stress curl integrated from the western coast of South America to the eastern coast of New Zealand or Australia. The white vertical line represents the zero of the integrated wind stress curl. Note that there is no zero in the integrated wind stress curl in the vicinity of New Zealand. It is always positive anticyclonic in the Southern Hemisphere with a maximum of 9.8×10^{-6} (Pa × 1°) m^{-1}.

tion, complete separation of a western boundary current from the coast occurs at the latitude of the zonally integrated zero wind stress curl line integrated from the eastern boundary to the western boundary segment. This separation can be complicated by land masses that partially block gyres and by gradients in the wind stress that give zonal currents but do not act as outer-gyre boundaries. There is no zero wind stress curl line (Fig. 6) that would cause the EAC to completely separate from the coast of Australia. A gradient, however, exists in the zonally integrated wind stress curl (shown as a gray line in Fig. 6) that causes a zonal flow eastward at 34°S, providing a southern boundary to a nested gyre within a larger gyre. The separation points of the EAUC (37°S) and the ECC (42°S) also correspond to gradients in the zonally integrated wind stress curl. Zonal currents at these latitudes are seen at the same latitudes, even after New Zealand has been removed (Fig. 5). The partial separation of the EAC can be explained by the response of the ocean to the wind field with New Zealand present or removed, suggesting that New Zealand does not affect the separation point, aside from the island's effect on the wind field itself. Since a reduced gravity model produces the correct EAC separation point, bottom topography and coastline details of Australia must also have little effect on the separation latitude.

The reversed direction of the EAUC in the linear simulation RG1 can be linked to higher than observed southward transport through the Tasman Sea. The simulated transport is slightly less than that of the linear model of Godfrey (1989), discussed in Ridgway and Godfrey (1994) (12.1 versus 15 Sv) but still larger than observations. Analysis of the mass balance of this region shows four pathways available for water to enter or exit the region (Fig. 7): the Tasman Sea, the basinwide transport at 32°S, the transport of the South Pacific subtropical gyre east of New Zealand at 39°S, and the western boundary current along New Zealand (i.e., the EAUC). Since net vertical mixing is small compared to the horizontal transports in this latitude band (32° to 39°S, marked in Fig. 7), the residual of the mass balance of the transports along the three other pathways determines the direction of the EAUC. If the non-EAUC transport into the region (equatorward flow of the South Pacific subtropical gyre across 39°S) is larger than that out of the region (transport across 32°S + Tasman Sea) then the EAUC must flow southeastward (out of the latitude band) to achieve mass balance. If the transport into the region is less than the transport out, the EAUC must be northwestward (into the latitude band). From Table 3, we can see that, if the EAUC is to flow southeastward in RG1, the southward flow through the Tasman Sea must be less than 9.0 Sv [25.5 (transport across 39°S) − 16.5 (transport across 32°S) = 9.0 Sv]. Since the simulated flow through the Tasman Sea in RG1 is larger than this value and the observed value, the simulated EAUC flows in the incorrect direction.

Decreasing the flow through the Tasman Sea in the linear simulation, to agree with observed values by increasing the local horizontal friction within the Tasman Sea (RG3) (Fig. 8a), produces an EAUC that flows southeastward, connecting the two northern inner gyres

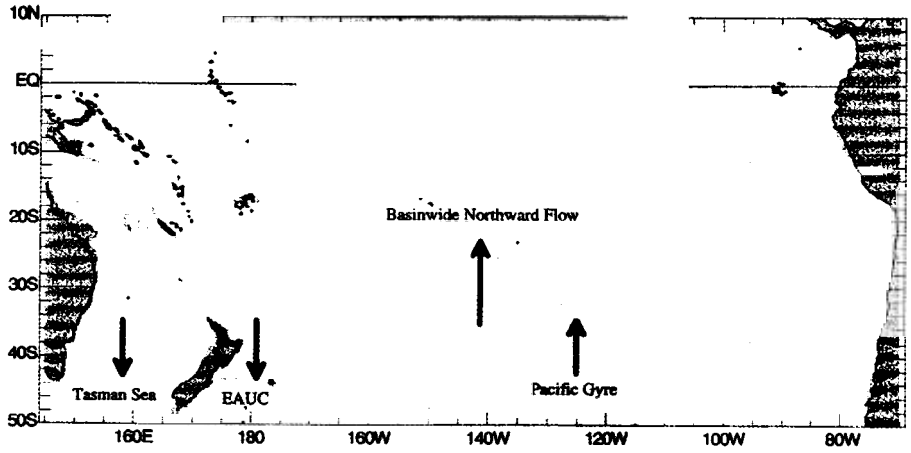

FIG. 7. Illustration of the mass balance of the region encompassing transport through the Tasman Sea, the Pacific Ocean at 32°S, the Pacific Ocean east of New Zealand at 39°S, and the East Auckland Current.

seen in Fig. 4b. The EAUC can be divided into two flow regimes: 1) before separation and 2) after separation. *Before separation* corresponds to the alongshore transport passing between the northern tip of New Zealand and 33.6°S, 176.5°E. *After separation* corresponds to the alongshore transport passing between the eastern coast of New Zealand and 36.0°S, 178.9°E, after the majority of the EAUC has turned offshore, leaving a much weaker flow attached to the coast (see Fig. 1). The linear EAUC from RG3 has a magnitude of 6.5 Sv before separation and 0.9 Sv after separation, in agreement with the lower bound of observations. The weaker attached flow continues around the East Cape and joins with a westward onshore flow to produce an ECC of 6.5 Sv. The separation point of the EAUC agrees well with observations and is situated at a sharp gradient in the zonally integrated wind stress curl (Fig. 6).

Since the model domain has no transport through the Bering Sea, all of the northward transport across the basin at 32°S must leave the basin through the IPT. Since estimates of the transport through the IPT vary from <5 to 18.6 ± 7 Sv (Godfrey 1996), an incorrect choice of a simulated IPT might conceivably affect the mass balance of our region. However, varying the magnitude of the IPT, and therefore the transport through 32°S, has no effect on the EAUC or ECC. Shutting off the flow through the IPT (RG4) does not change the total flow out of the region (Fig. 8b); it merely diverts the flow through the Tasman Sea via an increased EAC (42.4 versus 25.9 Sv) with no change in the EAUC or the ECC.

The failure of the linear model to produce the correct direction of the EAUC may be in part due to its inability to simulate isopycnal outcropping, which is discussed in the next section. Although the lowest-order response of the ocean to the wind stress can explain the direction and separation of most of the major currents in our region of interest, it fails to reproduce the complicated flow field to the north of New Zealand and the meanders in the Tasman Front.

b. Nonlinear dynamics: Flat-bottom case

A 6-layer nonlinear 1/8° simulation with a flat bottom (FB) driven by HR winds is employed to examine vertical structure and nonlinear dynamics. Mean surface currents calculated from the last four years of the simulation (Fig. 9a) reveal flow meanders in the Tasman Front and the relatively persistent eddies observed by Roemmich and Sutton (1998) north and east of New Zealand. The simulated surface currents reveal an elongated eddy corresponding to the observed NCE and eddies to the north and southeast of East Cape corresponding to the ECE and WE. The simulated meanders in the Tasman Front have wavelengths (~410 km) that agree with the observational values of 300–500 km (Stanton 1979; Andrews et al. 1980; and Mulhearn 1987) although their amplitude and phase do not.

Stanton (1976) postulates that the wavelengths of the meanders over the Norfolk Ridge might correspond to those of a westward-propagating Rossby wave, although there was not sufficient data at the time for a definite conclusion. Andrews et al. (1980) found that the wavelengths required for a Rossby wave with the observed propagation speed of the meanders were much larger than those observed and suggested that nonlinearities were affecting the flow. Both Stanton (1979, 1981) and Mulhearn (1987) mention the possibility of topographic influences on the meanders, although Mulhearn (1987) notes that he was unable to find a clear indication of the mechanism.

Several other authors have examined the dynamics behind stationary meanders associated with a separating western boundary current. Ou and De Ruijter (1986) argued that the exact separation point of a western boundary current was a function of the transport within

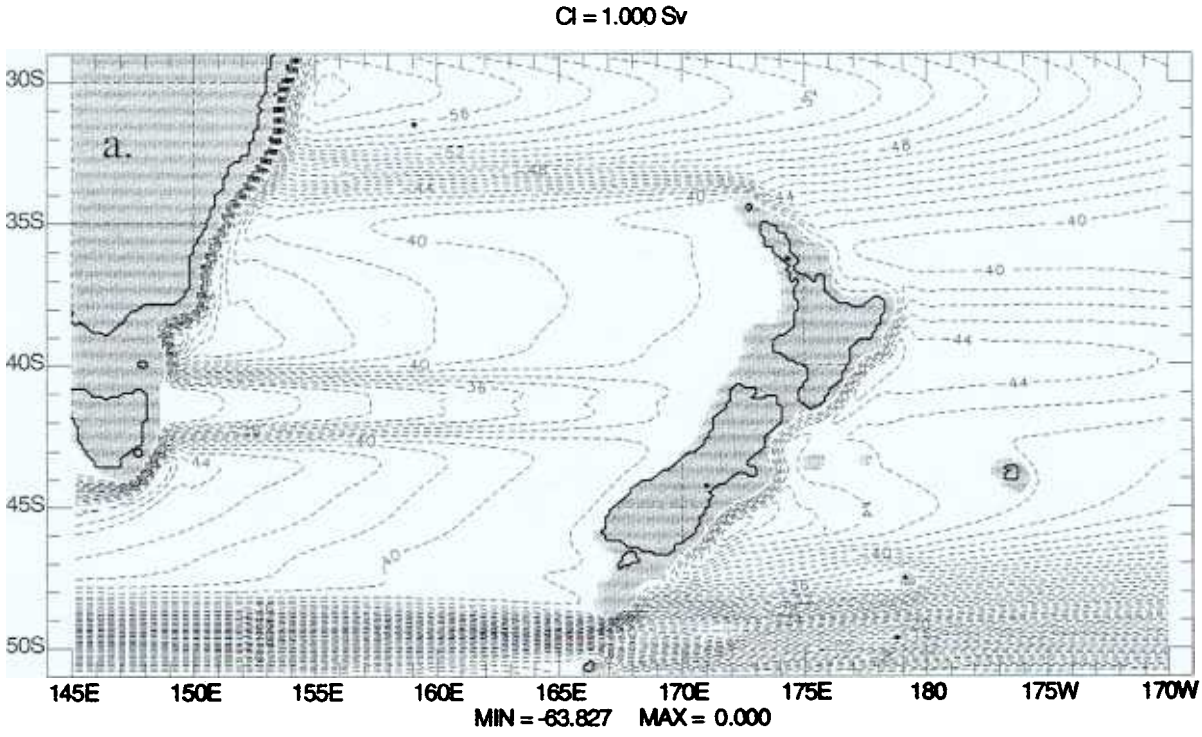

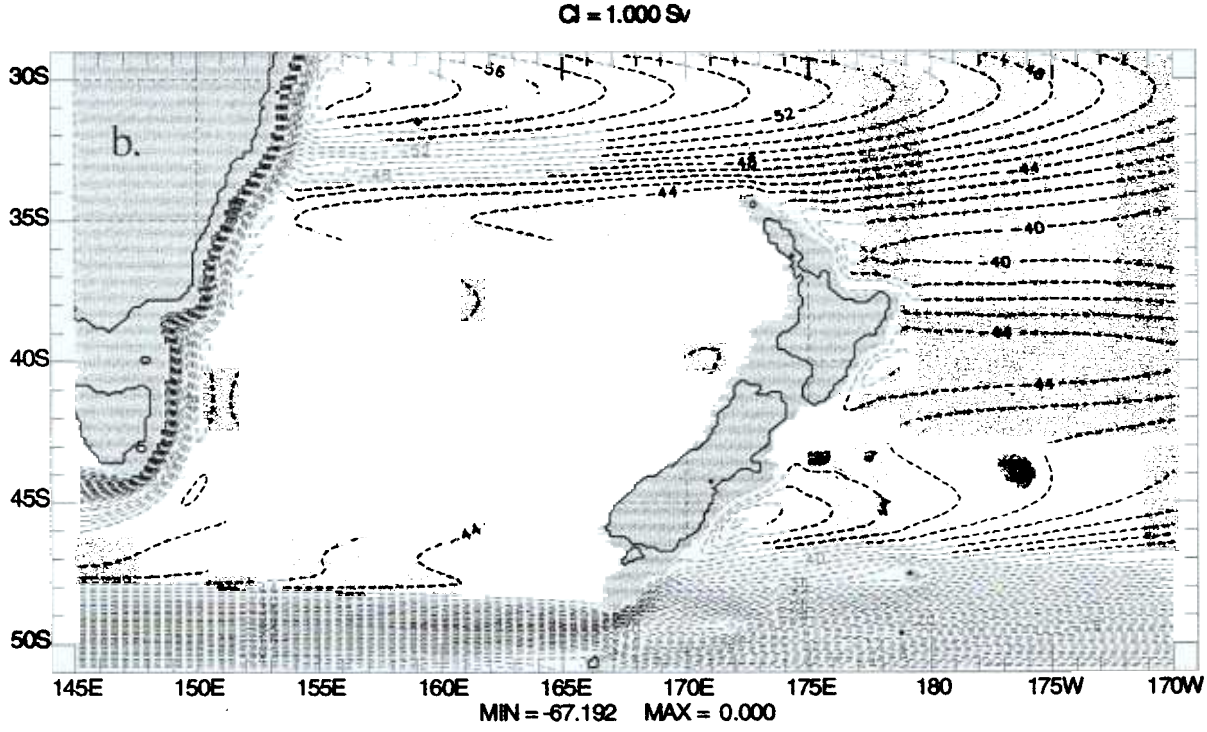

FIG. 8. Mean transport streamfunctions from the 1/8° linear 1.5-layer global simulations: (a) RG3, in which the horizontal friction in the Tasman Sea has been increased. Note the correct flow direction of the EAUC and correct separation points of all currents, except for the unobserved southward flow along the east coast of South Island. The small perturbation in the southern Tasman Sea is an effect of the friction patch and not of any changes in the winds. (b) RG4, in which the IPT has been closed off. Note the increased transport through the Tasman Sea and the continued northwestward direction of the EAUC.

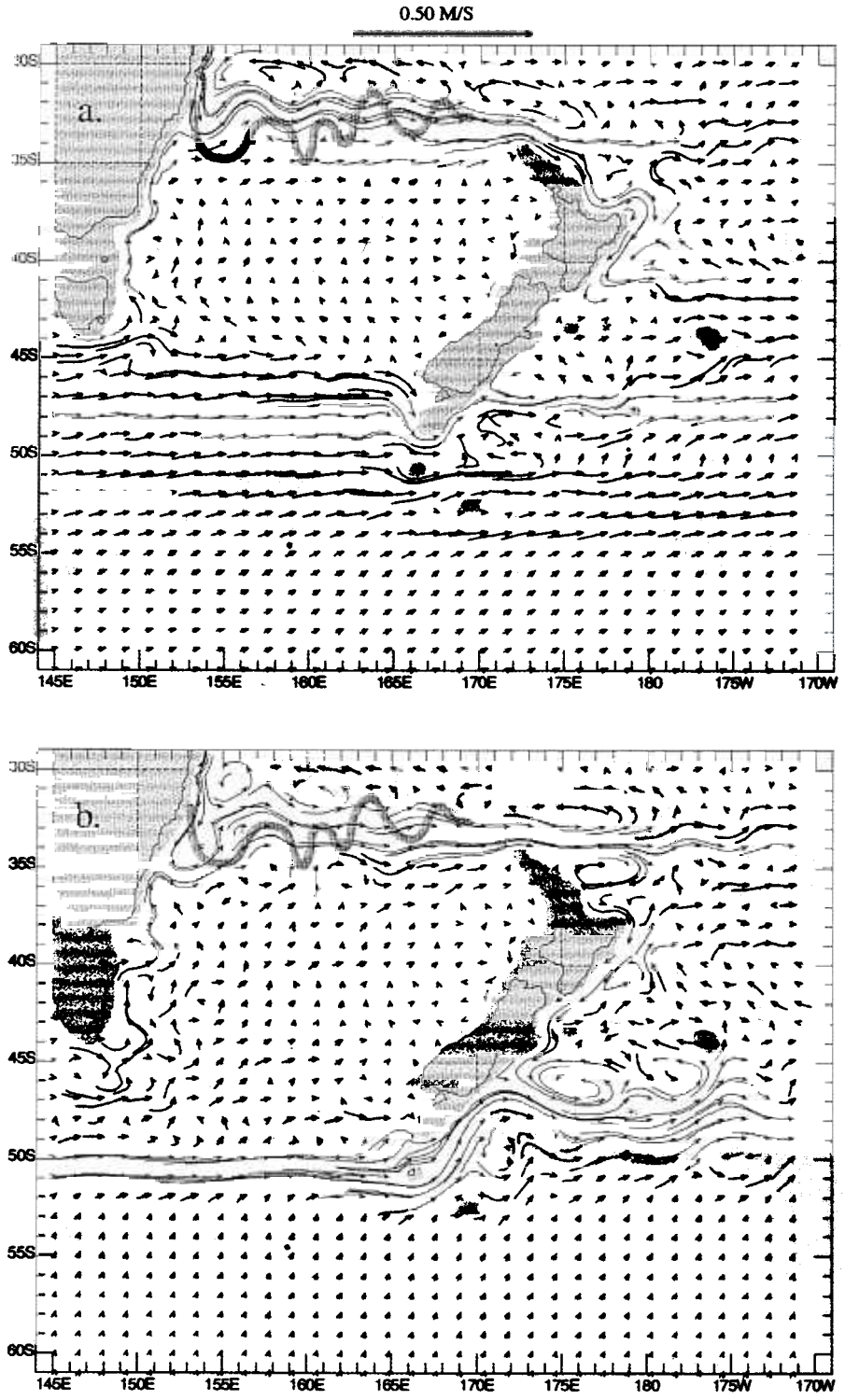

FIG. 9. Mean surface currents from the 1/8° nonlinear global simulations: (a) FB, the flat-bottom 6-layer simulation. The most probable Tasman Front pathway described in Fig. 2 is represented by the gray line in both figures. The mean currents were calculated from the last four years of the simulations. Note the mean meanders in the Tasman Front and the eddies north of New Zealand. The simulated meanders show poor agreement in phase with those observed and decrease in amplitude eastward along the Tasman Front contrary to observations. The ECC separates just north of the Chatham Rise as observed, even though there is no bottom topography to guide the flow. (b) RG5.5, the 5.5-layer reduced-gravity simulation. Note the lack of regular meanders, such as those found in FB, in the Tasman Front.

the current and the shape of the coastline. When the coastline slopes away from the separation point (similar to the orientation of the Australian coastline), the boundary current continues southward after separation and then retroflects to return to the latitude of initial separation, forming meanders that are then governed by conservation of absolute vorticity. Campos and Olson (1991) and Da Silveira et al. (1999) were both able to produce mean meanders in a zonal separation jet in both barotropic and baroclinic nonlinear simulations. Both sets of authors also found that the separation point and amplitude of the meanders were greatly influenced by the shape of the coastline. Holland (1978), using a quasigeostrophic 2-layer model with a straight western boundary did not reproduce meanders, demonstrating that some sort of asymmetry such as a sloped coastline is required to produce meanders.

The simulated meanders of the flat-bottom model (Fig. 9a) are approximately stationary, with the first meander extending southward and retroflecting northward, consistent with Ou and De Ruijter (1986), Campos and Olson (1991), and Da Silveira et al. (1999). The wavelengths of the meanders correspond to the most probable path discussed by Mulhearn (1987) and Stanton (1979) but the amplitudes or phase do not. The amplitudes of the simulated meanders decrease as the flow proceeds away from the western boundary as would be expected in an inertial flow, but in direct disagreement with observations. The wavelengths of both simulated (~410 km) and observed meanders (300–500 km) are less than those of a stationary Rossby wave pattern or constant absolute vorticity (CAV) trajectory (Haltiner and Martin 1957). For small amplitude trajectories, stationary wavelengths in CAV trajectories are related to the characteristic velocity of the flow by

$$\lambda = 2\pi\sqrt{\frac{v_c}{\beta}} \tag{4}$$

where v_c is the characteristic velocity at the core of the current and λ is the stationary wavelength.

The observed and simulated stationary wavelengths are less than the stationary wavelength (600 km) predicted from the depth-averaged velocity of the top five layers of FB (0.17 m s^{-1}). According to CAV theory, the simulated meanders should propagate eastward, not remain stationary as observed. When the bottom layer is constrained to be at rest, creating a 5.5-layer reduced-gravity simulation (Fig. 9b), the simulated meanders have longer than predicted stationary wavelengths and propagate westward, consistent with CAV theory. A long-term mean averages out these time-dependent features, resulting in a mean flow field with little or no meanders (Fig. 9b). Interestingly, the simulated EAC in the reduced gravity simulation separates farther south and retroflects northward to a larger degree than FB. The propagation in the reduced-gravity model and the stationarity in the flat-bottom model are clearly seen in a longitude–time plot of sea surface height deviation (Fig. 10). These differences suggest that, while the meanders within the reduced gravity model can be explained by CAV theory, other dynamics must be present in FB. The inclusion of the bottom boundary and, therefore the barotropic mode, allows the formation of baroclinic instabilities involving the barotropic mode within FB. The appearance in FB of meanders with wavelengths shorter than those predicted by CAV theory indicates that flow instabilities are shortening the wavelength of the mean meanders via vortex stretching. Evidence of the presence of baroclinic instabilities can be obtained by inspection of eddies formed from the meanders within the Tasman Front. The beta Rossby number, $R_b = v/\beta r^2$, is the ratio of relative to planetary vorticity advection, where v = maximum swirl velocity within the eddy and r = mean radius of the eddy. An R_b of order 1 suggests that the eddy was formed by barotropic instabilities involving the first baroclinic mode, while an R_b of order 10 suggests that it was formed by baroclinic instabilities involving the barotropic mode (McWilliams and Flierl 1979; Hurlburt and

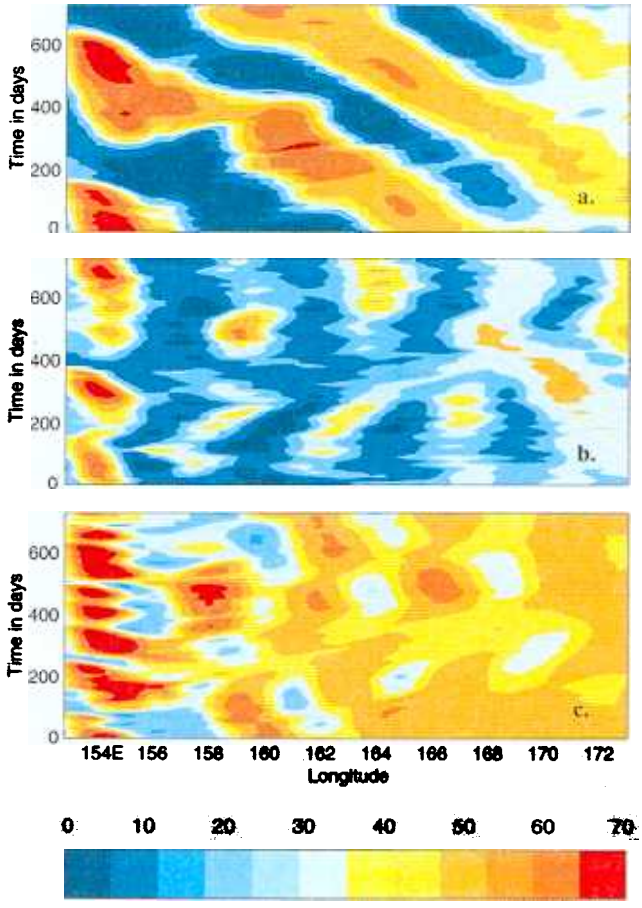

FIG. 10. Longitude–time plots of sea surface height deviations (cm) at 33°S from (a) RG5.5, (b) FB, and (c) RB8. These plots were calculated from the last two years of the simulations. Note the westward propagation of the signal in the reduced-gravity simulation and the stationarity in the two finite-depth simulations.

Thompson 1982, 1984; Murphy et al. 1999). Eddies formed during the last two years of the simulation (not shown) were characterized by $v \approx 35$ cm s^{-1} and $r \approx 47$ km, resulting in $R_b \approx 7.9$, suggesting that the eddies and, therefore, the meanders were formed by baroclinic instabilities.

Baroclinic instabilities may also be identified by the wavelength of the meanders within the flow field, since the growth rates of disturbances due to baroclinic instabilities are functions of the disturbance wavelength. Although the flow field is constantly exposed to disturbances of different wavelengths, it is predisposed to the propagation and growth of a limited range of wavelengths. Within a long-term mean of the flow field, stationary disturbances with large growth rates will dominate. Mean meanders produced by baroclinic instabilities will most likely exhibit the wavelength of these disturbances. Tilburg (2000), using an approach similar to Phillips (1954) and Haidvogel and Holland (1978), analyzed the susceptibility of the mean flow within FB to baroclinic instabilities by introducing to the mean layered vorticity equations a disturbance and solving for the growth rate. He found that the average wavelength within the simulated Tasman Front corresponded to a stationary, unstable disturbance, providing further evidence that the meanders are due to the presence of baroclinic instabilities.

The simulated directions and separation points of the investigated currents in FB generally agree with observations. Notably, the EAUC flows in the correct direction, while the ECC separates at 42°S and forms a broad band of eastward flow. However, the flow through the Tasman Sea in FB is no longer southward but is mostly confined to the western boundary and travels northward with a transport of 5.3 Sv. The confinement of a northward flow to the western boundary agrees with observations. Huyer et al. (1988), using both current meters and CTD/XBT surveys along the continental margin, found predominantly northward flow along the Australian shelf but southward flow in the interior of the Tasman Sea. The simulated surface flow is northward along the coast and slightly southward throughout the rest of the Tasman Sea, although the combined flow is northward, not southward as observed by Huyer et al. (1988) and others (Chiswell et al. 1997 and Ridgway and Godfrey 1997). The northward flow through the Tasman Sea combines with the EAC as it separates from the coast of Australia and flows eastward, producing significantly larger transports along the Tasman Front (31.6 Sv) than the linear simulations or observations. Although some transports greater than 30 Sv have been observed along the Tasman Front due to recirculation of the flow by eddies, time-averaged transports are much smaller (Stanton 1981). The simulated Southland Current also does not agree with observations.

Two mechanisms may contribute to the simulated northward transport through the Tasman Sea: unrealistically high IPT transport and exaggeration of the effect of isopycnal outcropping in reducing eastward baroclinic transport south of New Zealand. As mentioned in section 3a, any change in the transport through the IPT directly affects the transport at 32°S and through the Tasman Sea. An increased IPT would reduce the southward (or increase the northward) transport through the Tasman Sea but have little effect on the EAUC or the ECC. The introduction of isopycnal outcropping, however, significantly alters the nested gyres seen in the linear simulations. Isopycnal outcropping in the Antarctic region in response to the large negative wind stress curl (Fig. 6) reduces the transport passing south of New Zealand. The depths of the mean interfaces south of Australia and New Zealand (Table 4) are at a minimum along the coast of Antarctica, indicating significant outcropping. Within the model, an outcropped layer does not result in a zero thickness, but instead a minimum thickness. When all five upper layers in the hydrodynamic model outcrop (as is the case for the majority of the Antarctic region), only the nonsteric contribution to the barotropic transport remains, resulting in drastically reduced transport in the upper five layers. The mean interface depths at the coast of New Zealand are much shallower than those at the coast of Australia (Table 4), allowing less transport south of New Zealand than south of Australia, forcing transport northward through the Tasman Sea.

Returning to the linear simulation of the triple nested subtropical gyre system of the South Pacific (Fig. 4a), we see the impact of the reduced transport south of New Zealand on other current systems. Focusing on the middle-nested gyre in the southeast Pacific (represented by the dark green contour in Fig. 4a) we see flow associated with this gyre passing south of New Zealand. As this flow is reduced, more of it must pass north of New Zealand, impacting the transport through the Tasman Sea and the current system that comprises the Tasman Front, the EAUC, and the ECC. Since in FB the net transport through the Tasman Sea is northward, a portion of the supergyre transport feeding the IPT no longer passes south of New Zealand but instead flows north through the Tasman Sea and along the Tasman Front. To achieve mass balance in the latitudinal band described in Fig. 7, the EAUC now flows southeastward along the coast of North Island. The EAUC has a mean magnitude of 24.6 Sv before separation and 13.5 Sv after separation, both of which are significantly larger than those produced in the modified linear case (RG3) but still within the range of observational values.

Clearly the model overestimates the effect of isopycnal outcropping in this region, but it does reproduce the correct direction of the EAUC, suggesting that the dynamics of isopycnal outcropping, if not the magnitude of its simulated effect, are correct. The exaggerated effect of this outcropping on the transport of the ACC has been noted earlier. Shriver and Hurlburt (1997), using a lower-resolution version of this model, found that the simulated transport of the ACC through the Drake Pas-

TABLE 4. Shown are mean interface depths (m) at land boundaries south of Australia and New Zealand. Note that the interface depths at the coast of Australia are greater than those at New Zealand, providing greater transport south of Australia than New Zealand and forcing northward transport through the Tasman Sea. The initial depths of the mean interfaces of RB8 and RB16 are different from those of FB (i.e. interface 5 for FB is 1000 m, while interface 5 for RB8 and RB16 is 1500 m). These differences affect the extent of isopycnal outcropping on the interfaces and, therefore, the available transport south of New Zealand and Australia.

Experiment	Interface	Antarctica at 167.84°E	New Zealand at 167.84°E	Antarctica at 146.92°E	Australia at 146.92°E
		51	107	51	212
		91	268	91	383
FB		131	515	130	647
		170	785	170	951
		210	1140	210	1171
		51	157	52	231
	2	92	363	92	375
RB8	3	132	711	132	719
	4	172	1234	172	1143
	5	212	1718	212	1701
		52	137	52	227
	2	93	300	93	371
RB16	3	135	679	133	724
	4	176	1143	174	1150
	5	218	1581	214	1676

sage was much less than observed values and attributed this difference to the effect of the modeled isopycnal outcropping.

The linear model RG1 does not reproduce isopycnal outcropping and therefore must be modified to reproduce the reduced flow (RG3) through the Tasman Sea and the observed direction of the EAUC. A model that incorporates isopycnal outcropping (FB) does reproduce the observed direction of the EAUC. The flat-bottom simulation also produces meanders with wavelengths that agree with observations but phases and amplitudes that do not.

c. *Nonlinear dynamics: Realistic bottom topography case*

A 6-layer nonlinear 1/8° simulation with realistic bottom topography (RB8) is used to investigate the role of upper-ocean–topographic coupling in this region. Mean surface currents superimposed on bottom topography (Fig. 11) show that the simulation reproduces stationary meanders (Fig. 10) in the eastern portion of the Tasman Front (meanders E, F, and G, in Fig. 2), the phase of which more closely agrees with observations, revealing the importance of upper-ocean–topographic coupling. The simulated EAC separates slightly farther south than FB (35° versus 32°S) and creates a large retroflection similar to the reduced gravity simulation. RB8 also reproduces all three quasi-stationary eddies and the low observed by Roemmich and Sutton (1998) north and east of the North Island of New Zealand. In RB8, the simulated surface ECC separates from the coast of New Zealand and flows eastward south of the Chatham Rise rather than north of the rise as seen in observations and the other simulations. A summation of the five top layers (not shown) shows a zonal current at the observed latitude of 42°S, revealing the baroclinic nature of the flow and depth-integrated agreement with observations. The introduction of the bottom topography greatly reduces the northward transport through the Tasman Sea (0.1 versus 5.3 Sv), while increasing the IPT transport (13.7 versus 10.5 Sv). These changes combine to produce a reduced transport in the Tasman Front (23.1 versus 31.6 Sv). Although mass balance of the region still requires the EAUC and ECC to proceed southward, the decrease in the Tasman Sea transport gives a smaller transport in both the after separation EAUC (3.8 versus 13.5 Sv) and the ECC (11.7 versus 14.9 Sv). The simulated Southland Current flows in the observed direction, revealing that its location is determined by bottom topography.

The major differences between FB and RB8 are the incorporation of bottom topography, which introduces a bottom layer that is constrained to follow f/h contours, and the change in the initial depth of the mean interfaces. The introduction of bottom topography has two major ramifications: 1) reduction of baroclinic instabilities and 2) bottom steering. When the bottom layer is constrained by topography, it cannot freely adjust to perturbations and become out of phase with the surface layer. This restriction reduces the distribution of baroclinic instabilities and their potential for occurrence. Baroclinic instabilities convert potential energy of the mean flow to eddy potential energy, effectively flattening mean isopycnals. Since transport is related to the change in depth of isopycnals via the thermal wind relation, this flattening restricts the transport south of New Zealand. The greater depth of the original interfaces in RB8 (1500 m for interface 5) compared to FB (1000 m for interface 5) mitigates some of the effect of isopycnal outcropping and provides greater potential for transport south of New Zealand and Australia. The decrease of baroclinic instabilities and the increase in initial inter-

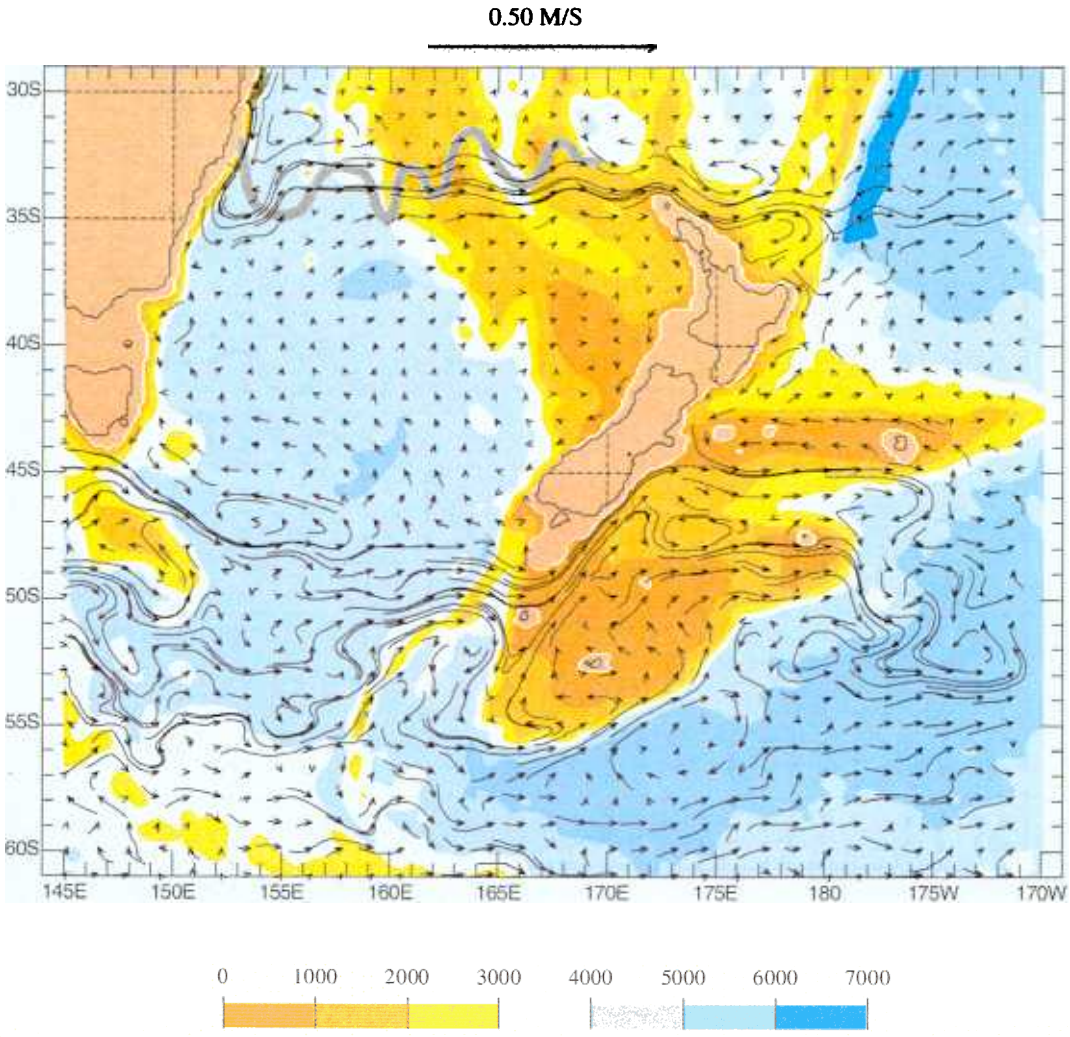

FIG. 11. Mean surface currents from the 1/8° nonlinear 6-layer simulation, RB8 superimposed on the model bottom topography (m). Note the correct placement of the meanders in the eastern portion of the Tasman Front and the presence of the eddies north of New Zealand as well as reduced flow through the Tasman Sea compared to FB.

face depth result in much deeper ispoycnals south of Australia and New Zealand in RB8 than FB (Table 4). The relative deepening of the isopycnals allows more transport south of New Zealand, and, consequently, decreases the northward flow through the Tasman Sea.

The inclusion of bottom topography can substantially affect surface currents that do not directly impinge on the topography. Hurlburt and Metzger (1998) found indications of the Shatsky Rise topography affecting the bifurcation of the Kuroshio. This steering is due to the abyssal currents advecting upper-layer thickness gradients and, therefore, surface currents.

Conservation of potential vorticity is a sufficient constraint to allow even deep low-amplitude topographic features to steer the abyssal flow. Hurlburt and Thompson (1980, 1982, and 1984) used the continuity equation to demonstrate how upper-ocean currents can be driven by abyssal flow. In a two-layer model it can be shown that the two-layer velocities are linked by

$$\mathbf{v}_{1_g} \cdot \nabla h_1 = \mathbf{v}_{2_g} \cdot \nabla h_1, \tag{5}$$

where $\mathbf{v}_{k_g}$ is the geostrophic velocity in layer k. The left-hand side of (5) is the geostrophic contribution to the advective term in the continuity equation (3) for layer 1. Additionally, the geostrophic balance of the internal mode in a two-layer model is given by

$$\mathbf{k} \times f(\mathbf{v}_{1_g} - \mathbf{v}_{2_g}) = -g' \nabla h_1, \tag{6}$$

where $g' = g(\rho_2 - \rho_1)/\rho_0$. When the surface currents are much larger than the abyssal currents ($|\mathbf{v}_{1_g}| \gg |\mathbf{v}_{2_g}|$), which is typically the case in a two-layer model, Eq. (6) indicates that ∇h_1 can be used as an approximate measure of $\mathbf{v}_{1_g}$. From this observation and the combined effects of (5) and (6), we see that the abyssal currents advect upper-layer thickness gradients and, therefore, steer upper-layer currents. Hurlburt et al. (1996) showed that, although this theory formally breaks down in the multilayer case, this steering effect remains when the

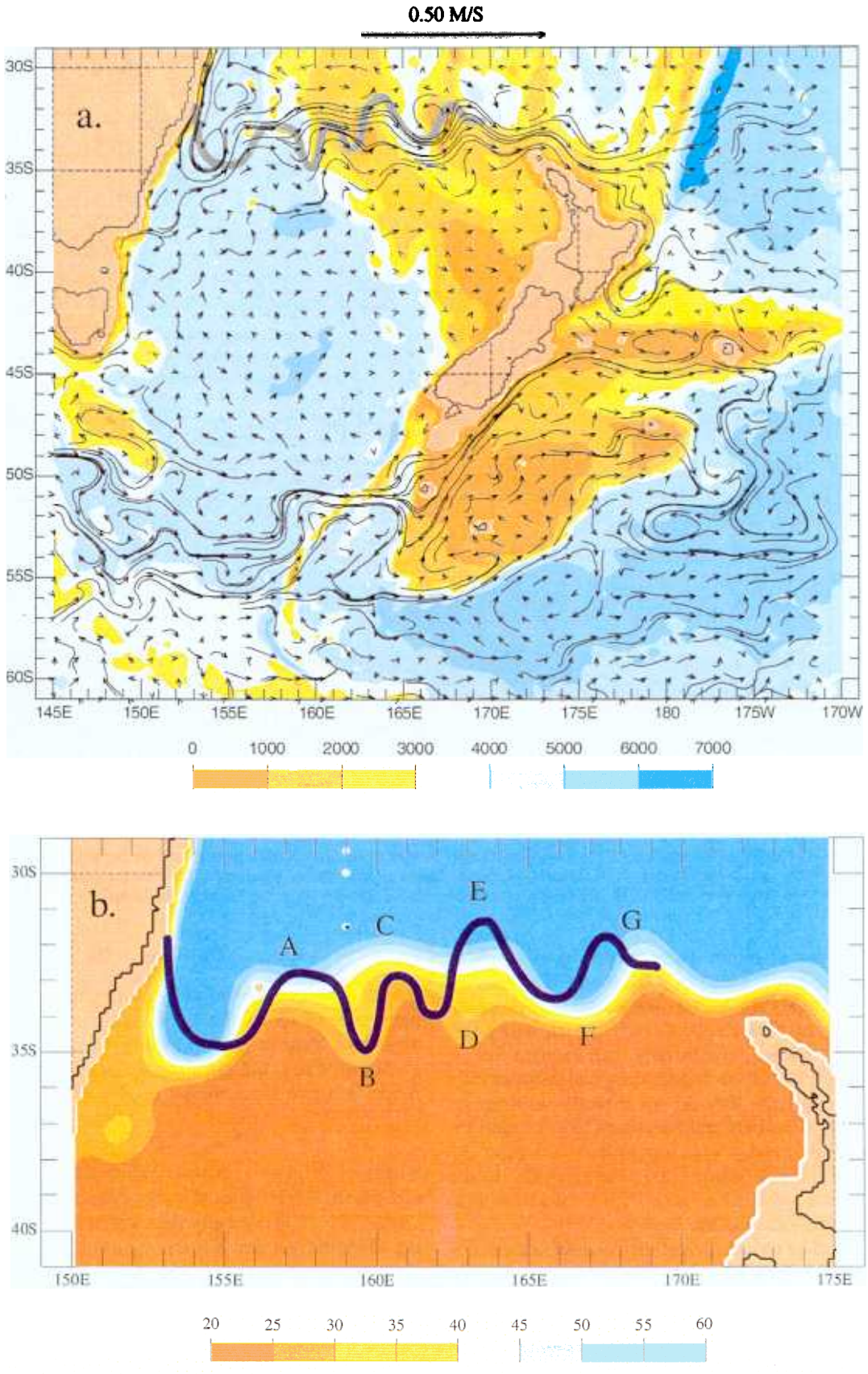

FIG. 12. (a) Mean surface currents from the 1/16° nonlinear 6-layer simulation, RB16 superimposed on the model bottom topography (m). Note the larger meanders in the Tasman Front and the presence of the NCE and WE. The

first baroclinic and barotropic modes dominate the flow regime, a valid assumption in our region of interest.

As discussed in the previous section, the presence of baroclinic instabilities in FB regulates the wavelength of the meanders in the Tasman Front. The effect on the meander wavelength of the decrease of baroclinic instabilities due to the inclusion of bottom topography in RB8 is compensated by bottom steering, resulting in meanders that are similar in wavelength to those in FB but have a phase that now agrees more closely with observations. Inspection of the bottom topography (Fig. 2) beneath the Tasman Front reveals a series of ridges and valleys, which constrain the abyssal flow and affect the surface flow. Since the presence of bottom topography does not allow the abyssal layer to freely adjust and create meanders solely due to baroclinic instabilities, the wavelengths of the meanders are not directly determined by the presence of the instabilities themselves, although the instabilities may provide a length scale for the meanders. Instead, the flow instabilities contribute energy to the abyssal layer providing greater bottom steering, which determines the wavelengths.

Increasing the resolution of RB8 to 1/16° (RB16) (Fig. 12a) significantly increases the amplitude of the meanders in the entire Tasman Front and produces meanders in the western portion (meanders A, B, C, and D, in Fig. 2) that agree quite well in phase, amplitude, and wavelength with observations. Comparison of the mean sea surface deviations of the model and the most probable path from Fig. 2 (Fig. 12b) demonstrates that the simulation resolves each observed meander. The increased resolution in RB16 increases the northward transport through the Tasman Sea (6.4 versus 0.1 Sv) with little effect on the IPT and strengthens the EAUC (8.5 versus 3.8 Sv) and the ECC (15.9 versus 11.7 Sv). The quasi-stationary eddies corresponding to the Wairarapa Eddy and the NCE are evident, but in the mean the ECE and the low have merged. Uddstrom and Oien (1999) were also unable to detect a robust ECE in their SST fields, indicating a high amount of variability in this region. The closer agreement of the simulated meanders with observations suggests stronger upper-ocean–topographic coupling in RB16 than in RB8.

Preliminary results from a further increase in resolution to 1/32° (Fig. 13) shows very little difference between the 1/16° and 1/32° simulations in the vicinity of the Tasman Front. This simulation was initialized from simulation RB16 and extended 8 years at 1/32° resolution and, hence, is not completely equilibrated at this resolution but is sufficiently equilibrated to show the impact of the increase in resolution on flow instabilities and therefore the mean meanders within the Tasman Front. The agreement between the two simulations in the Tasman Front suggests that the simulation has reached a convergent solution, and the flow features are not functions of resolution. The disagreement between the two simulations in the region north of New Zealand (Figs. 12a and 13) should be expected since within this region both simulations exhibit a large degree of variability and should not be considered inconsistent with the convergence of the simulations.

The simulated sea surface height variability of RB16 qualitatively agrees with TOPEX/Poseidon altimeter data (Fig. 14). The peak values of variability in the EAC and New Zealand region (the separation point of the EAC, along the Tasman Front, and directly north and east of North Island) are colocated in the simulations and the observations and can be directly linked to physical phenomena. The large variability in the region of the EAC separation is due to both the seasonal migration of the separation point and eddy shedding, while the large amount of variability along the Tasman Front indicates significant movement of the meanders. The large variability north and east of North Island can be linked to the presence of the quasi-stationary eddies and meandering of the EAUC and ECC.

Since the model is hydrodynamic and forced by monthly a wind stress climatology and the actual ocean is subject to seasonal thermal forcing and high-frequency winds, the overall variability of the model is less than that measured by TOPEX/Poseidon. Lower modeled SSH variability in locations such as east of Tasmania and within the southern section of our region of interest is expected. However, while the simulated variability north of New Zealand agrees qualitatively with observations, it is significantly higher than observations. The disagreement between the model and observations can be linked to the model's inability to adequately resolve the transport south of New Zealand and Australia. As discussed in section 3b, the reduction of flow south of New Zealand due to the model's insufficient vertical resolution in that region forces northward flow through the Tasman Sea, resulting in an unrealistically large current associated with the Tasman Front and therefore the EAUC. Instabilities and meanders within these unrealistically large currents result in larger than observed SSH variability as seen in Fig. 14. Examination of the SSH variability of the lower-resolution RB8a (not shown) reveals less variability throughout our region of interest and much less variability north and east of New Zealand. The decreased variability north and east of New Zealand in RB8a is consistent with our explanation of the origin of the SSH variability, since RB8a contains much smaller transports within the Tasman Front, EAC, and ECC. The location of the observed ECE is a region of extremely high variability in

←

ECE has merged with the low, obscuring both features. (b) Most probable path of the Tasman Front superimposed on the mean sea surface height deviation (cm) of RB16. Note the close match between the observed and simulated Tasman Front.

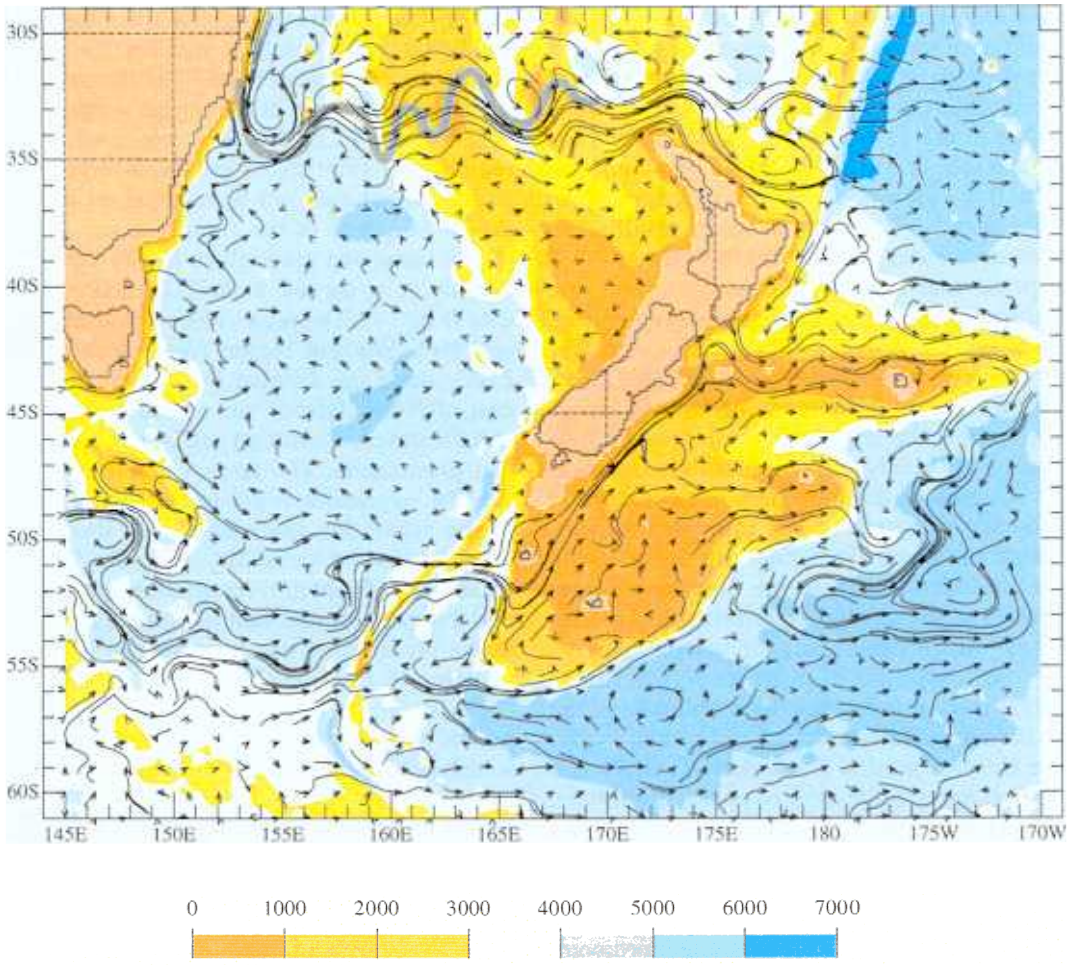

FIG. 13. Mean surface currents from a 1/32° nonlinear 6-layer simulation, RB32 superimposed on the model bottom topography (m). Note the good agreement between the RB16 and RB32 in the vicinity of the Tasman Front but poorer agreement in the vicinity of the highly variable region north of North Island.

the model and observations, providing a possible explanation for the mixing of the low and the ECE in RB16.

Maps of surface and abyssal eddy kinetic energy (EKE) from RB8 and RB16 (Fig. 15) demonstrate that the energy in both the surface and abyssal layers increases with this increase in grid resolution. The increased resolution in RB16 allows greater flow instabilities and an increased rate of energy transfer to the abyssal layers via these instabilities. Hogan and Hurlburt (2000) provide a clear discussion and illustration of the vertical transfer of energy. A mean value of R_b for eddies produced by RB16 is 6.9, which is slightly lower than FB, suggesting that the eddies' formation may be due to mixed barotropic–baroclinic instabilities. In fact, latitude–time plots of the meridional derivative of the barotropic absolute vorticity (dQ/dy) at 165°E (Fig. 16) show that the derivative changes sign frequently within our domain, which is a necessary (but not sufficient) condition for barotropic instability and suggests that barotropic instabilities are probable in this region.

Although mixed barotropic–baroclinic instabilities are very efficient mechanisms for transferring energy from the surface layers to the abyssal layers, other mechanisms may also drive abyssal EKE, such as vertical mixing or direct barotropic forcing by temporal variations in the wind stress. Very little vertical mixing between the surface and abyssal layers occurs in the area of the Tasman Front and New Zealand, although a significant amount does occur south of New Zealand. The collocation of EKE maxima in the surface and abyssal layers combined with the increase in variability with resolution is clear evidence that instabilities are present (Holland and Lin 1975) and that they, and not a barotropic response to the seasonal wind variations, are the major source of abyssal EKE (Hurlburt and Metzger 1998). The increase in baroclinic instability in RB16 over RB8 reduces the depth of the isopycnal trough north of the ACC as a result of the increased transfer

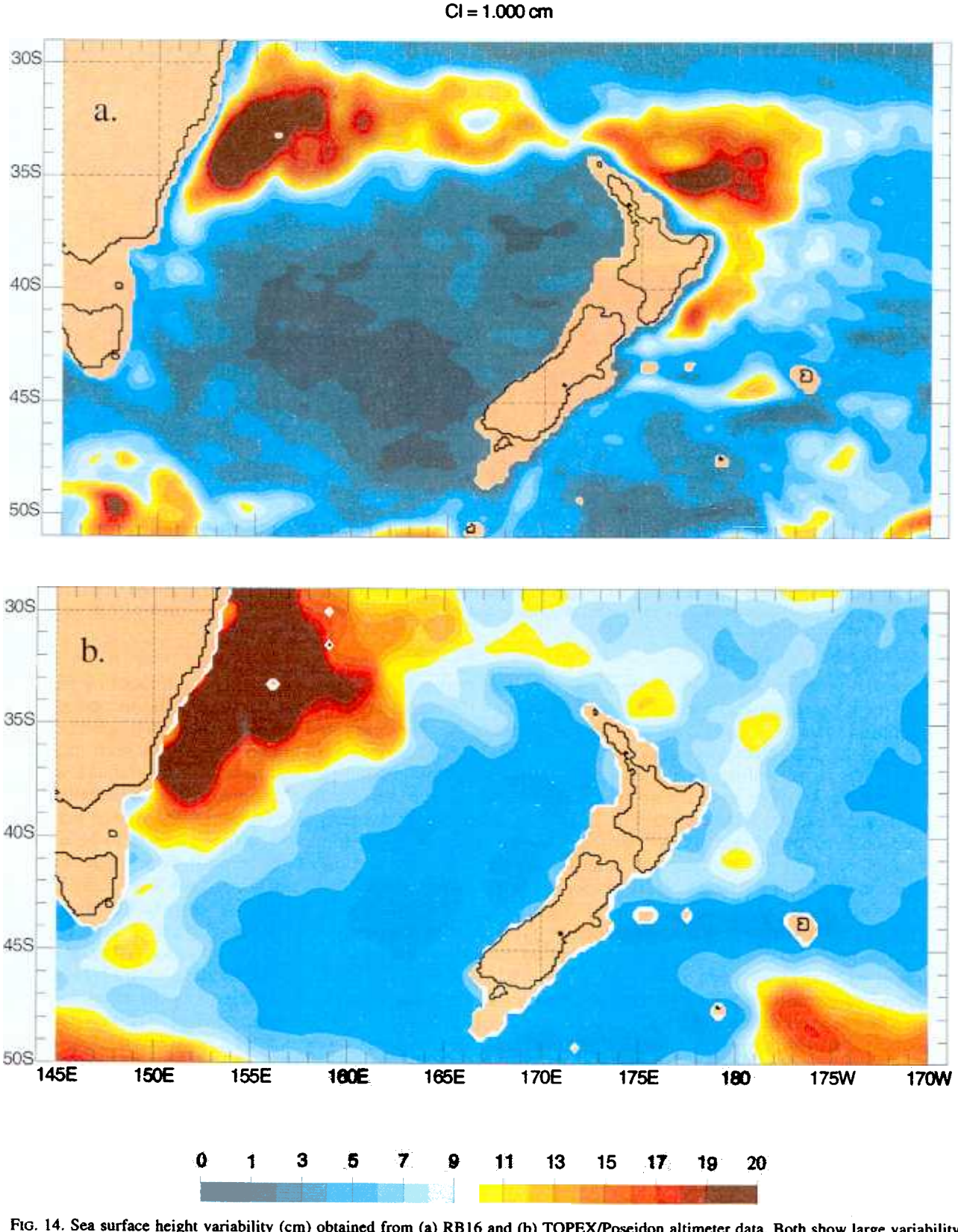

FIG. 14. Sea surface height variability (cm) obtained from (a) RB16 and (b) TOPEX/Poseidon altimeter data. Both show large variability at the EAC separation point. RB16 exhibits large variability of the flow field north and east of North Island. While the observed data show qualitative agreement in the variability pattern of the SSH around North Island, it is much lower in amplitude.

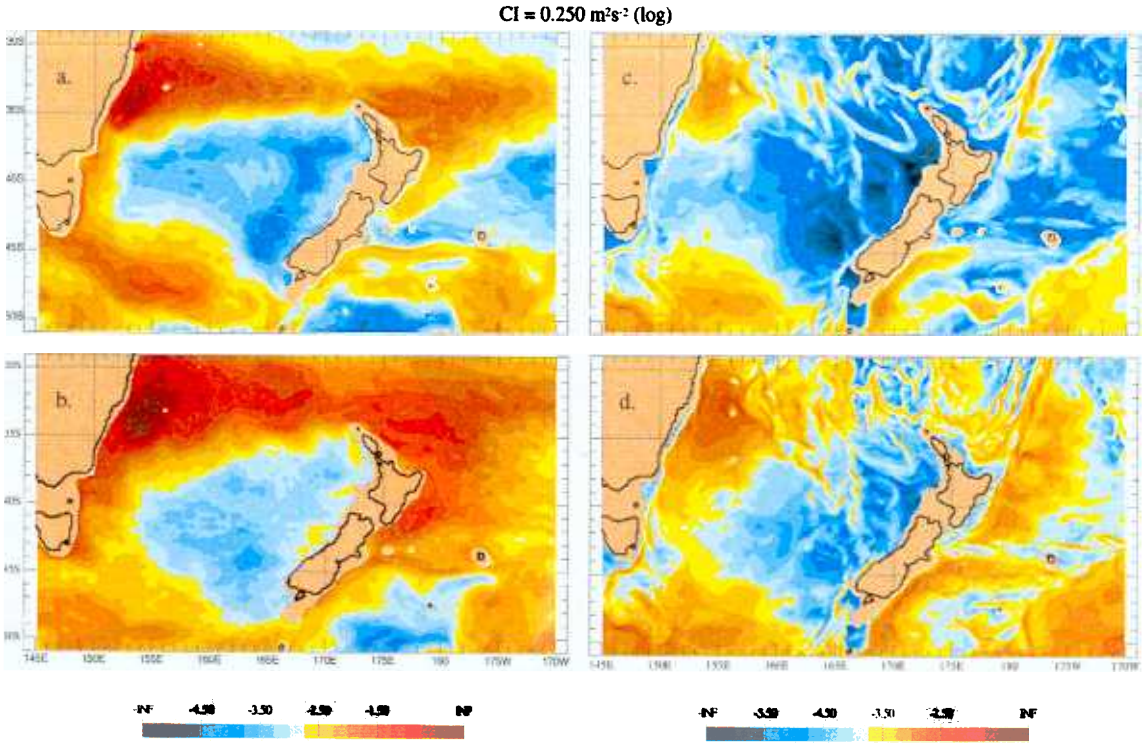

FIG. 15. Mean surface-layer eddy kinetic energy (EKE) of (a) RB8 and (b) RB16 and abyssal-layer EKE of (c) RB8 and (d) RB16. The contour interval is 0.25 $m^2 s^{-2}$ (log). Note the change in color bar between surface and abyssal layers. The energies of both layers increase as the resolution increases and the surface- and abyssal-layer EKE are colocated, both signs of baroclinic instabilities.

between the potential energy of the mean flow to the eddy potential energy and consequent isopycnal flattening (reduced range of temporal mean isopycnal depths in the region). This flattening reduces the mean isopycnal depths at the southern tips of Australia and New Zealand (Table 4), more so at the southern tip of New Zealand, which extends farther south (Fig. 2). In all cases the isopycnals outcrop at Antarctica (reach the minimum depth allowed in the model). Since all other factors are invariant in RB8 and RB16, the relative magnitude of the baroclinic transport through sections is determined by the isopycnal depth ranges across the sections. Thus, the results in Table 4 show greater restriction on the baroclinic ACC transport south of New Zealand in RB16 and therefore increased northward transport through the Tasman Sea in accord with Table 2.

The link between abyssal energy and upper-ocean–topographic coupling can be clearly seen. Large amounts of abyssal energy are collocated with bottom steering of upper-ocean currents such as the meanders in the Tasman Front (Figs. 11, 12, and 15). RB16 with a larger amount of abyssal energy and, therefore, more energetic abyssal currents, produces more bottom steering and larger meanders than RB8. The increased variability and barotropic–baroclinic instabilities enable more upper-ocean–topographic coupling in the higher-resolution simulation. For this reason, we use these simulations to investigate in detail the role of several topographic features in steering the surface flow field. Two separate areas merit discussion: the meanders of the Tasman Front and the apparent bottom steering of the ECC over the Hikurangi Trench. As seen in Fig. 12, many surface features appear to be coupled with particular topographic features. Topographically driven abyssal currents intersecting with surface currents at large angles force the surface currents to be displaced in the direction of the abyssal flow where the flows overlay (Hurlburt and Thompson 1980, 1982, 1984). The surface currents tend to return to the same latitude after the perturbation by the abyssal currents, consistent with potential vorticity conservation. Abyssal currents superimposed onto the sea surface height contours (Fig. 17) show that all meanders, with the exception of the first, of the Tasman Front are associated with meridional abyssal flow on the side of a ridge or a trough. The first meander is consistent with the separation overshoot and retroflection described by Ou and De Ruijter (1987). Two meanders discussed by Stanton (1979), the large southward meander located at the New Caledonia Trough (166°E, meander F) and the northward meander over Norfolk Ridge (167°E, meander G) are both driven by meridional flows along ridges. Abyssal currents also drive meanders documented by Mulhearn (1987) that are associated with the Dampier Ridge (159°E, meander B) and Lord Howe Rise (161°E, meander E). While the directions of meanders A, C, E, F, and G might be ex-

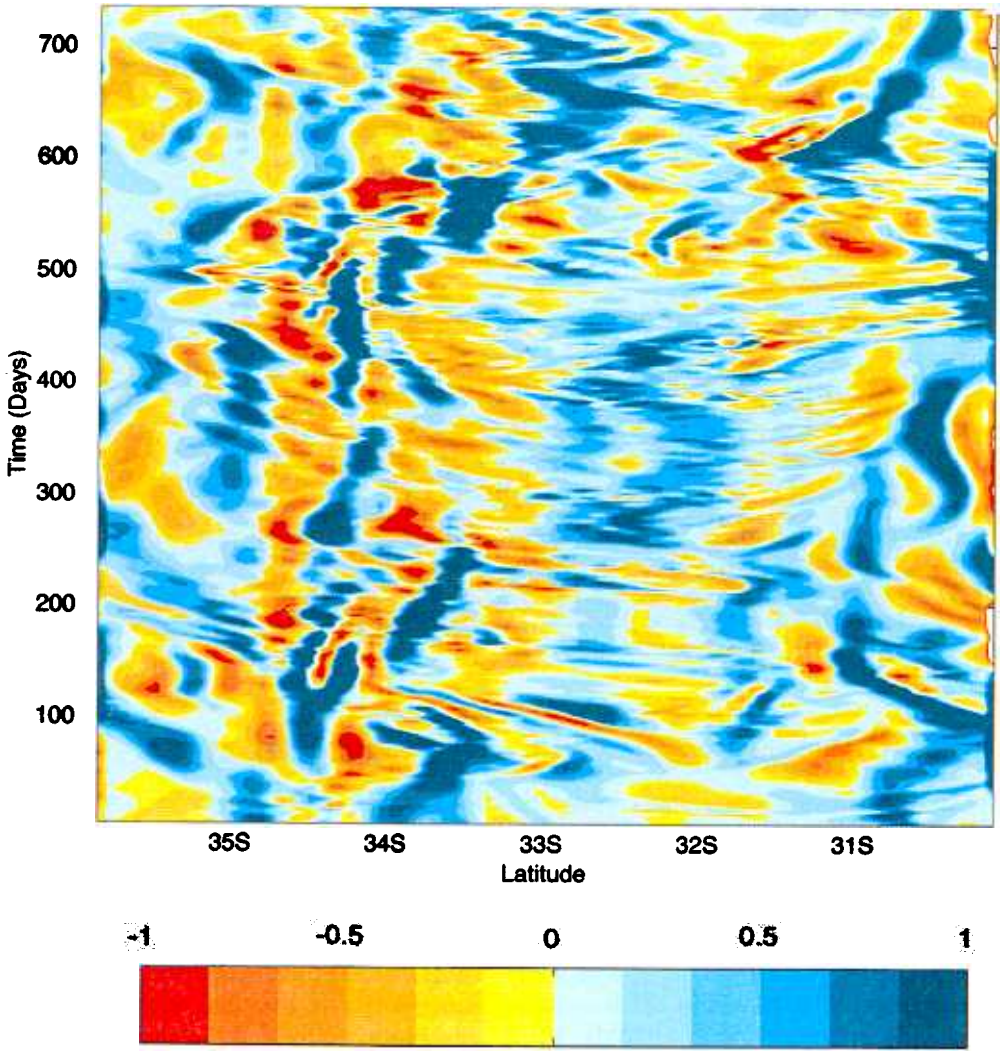

FIG. 16. Latitude–time plot of normalized dQ/dy at 165°E from RB16, where Q is the barotropic absolute vorticity. Note the change in sign, a necessary condition for barotropic instabilities.

pected from conservation of potential vorticity of a barotropic flow, Stanton (1979) clearly shows that the flow associated with the Tasman Front is highly baroclinic. Also, the southward meanders located directly east of Dampier Ridge (meander B) and on the western side of the Lord Howe Rise (meander D) are opposite in direction to those predicted by conservation of potential vorticity. However, the corresponding simulated meanders are directly above southward abyssal flow along the ridge, which forces the surface flow to form southward meanders.

At first glance, the flow of the ECC appears to be governed by the Hikurangi Trough. It separates very near to the location of the Chatham Rise and apparently follows this ridge line. In fact, the separation point in the realistic bottom topography simulations is the same as the flat-bottom model. As mentioned in section 3a, the separation is governed by the integrated wind stress curl and not bottom topography.

From examination of the simulations we are able to determine the governing dynamics behind several features of the flow field surrounding New Zealand. Upper-ocean–topographic coupling via baroclinic instabilities governs the phase and amplitude of the mean meanders in the Tasman Front. The flat-bottom nonlinear model and even the linear model with the added friction patch produce the correct directions and separation points for all examined currents. The shape of the wind stress curl and not bottom topography determines the separation points of these currents.

4. Summary and conclusions

Global ocean models with increasing dynamical complexity are used to investigate the dynamics of the East Australian Current, the Tasman Front, and the flow field directly north and east of New Zealand. The simulations have horizontal resolutions of 1/8°, 1/16°, or 1/32° for

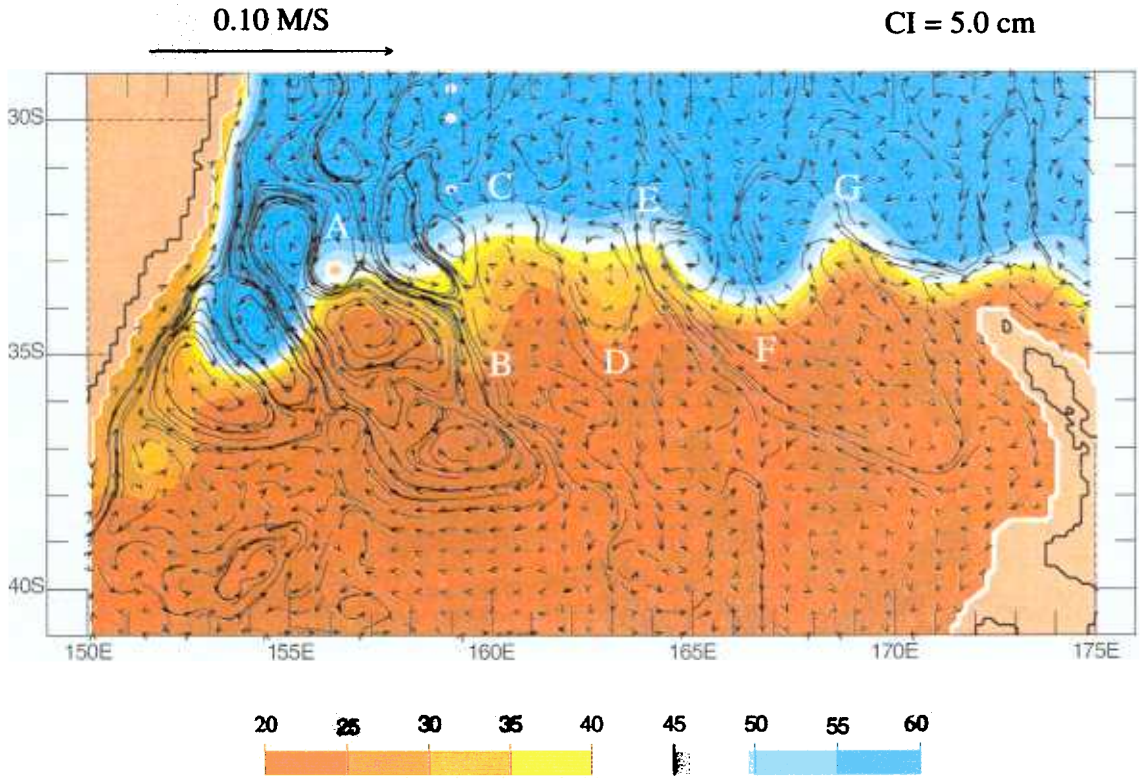

FIG. 17. Mean abyssal-layer currents (black arrows) from the 1/16° nonlinear 6-layer simulation with realistic bottom topography, RB16, superimposed on mean sea surface deviations (cm) in the vicinity of the Tasman Front. Note the steering of the surface-layer meanders by the abyssal flow.

each variable and vertical resolutions ranging from 1.5-layer reduced gravity to 6-layer finite depth with realistic bottom topography. All simulations are forced by the Hellerman and Rosenstein (1983) monthly wind stress climatology and were spun up to statistical equilibrium at 1/2° and 1/4° resolutions before continuing at the higher resolutions.

Analysis of these simulations demonstrates that several factors play a critical role in governing the behavior of the EAC, the Tasman Front, the EAUC, and the ECC. These factors include 1) mass balance of water pathways through the area, 2) gradients in the wind stress curl field, 3) nonlinear flow instabilities, and 4) upper-ocean–topographic coupling due to mixed baroclinic and barotropic instabilities. The increased variability of the increased-resolution simulation contributes greatly to topographic steering of surface currents that do not directly impinge on the bottom topography.

The transport streamfunctions for a linear reduced gravity model representing the first-order response of the ocean to the wind stress show a series of nested gyres in our region of interest. A supergyre spans the entire Southern Hemisphere; a smaller gyre encompasses the South Pacific Ocean; and three even smaller gyres are bounded on the west by Australia and New Zealand. The EAC and ECC are western boundary currents of the gyres, while the EAUC provides non-Sverdrup mass transport between two gyres defined by Sverdrup flow. The Tasman Front is the southern arm of the innermost gyre bounded on the west by Australia. The separation latitude of the simulated linear EAC agrees well with observations, with New Zealand present or removed, suggesting that the separation point is due to the shape of the wind stress curl and not the presence of New Zealand or bottom topography. Although the linear model reproduces the large-scale features well, it overestimates the southward transport through the Tasman Sea and produces an EAUC flowing opposite to that observed, suggesting that the Sverdrup response of the ocean cannot fully describe the flow in our region of interest. The flow through the Tasman Sea is directly linked to the direction of the EAUC. Mass balance demonstrates that the southward flow through the Tasman Sea must be less than the difference between the basinwide flow at 32°S and the northward flow east of New Zealand at 39°S to simulate an EAUC flowing in the observed direction. Decreasing the flow through the Tasman Sea by increasing the local horizontal friction produces a modified linear EAUC flowing in the correct direction. With this decrease all examined currents flow in the correct direction and separate from the coastlines at the observed locations. However, a simulation incorporating vertical structure is required to investigate

the dynamics that modify the transport through the Tasman Sea.

A nonlinear 6-layer flat-bottom simulation produces currents flowing in the observed direction and separating from the coastlines at the observed latitudes. It also produces meanders in the Tasman Front, the observed quasi-stationary eddies north and east of New Zealand, and isopycnal outcropping. The wavelengths of the simulated meanders in the Tasman Front agree well with observations, but their phase and amplitude do not. The wavelengths are shorter than those predicted by constant absolute vorticity theory, indicating that flow instabilities (particularly baroclinic instabilities), via vortex stretching, determine the wavelength. The simulated transport through the Tasman Sea is northward, in disagreement with observations, resulting in a transport associated with the Tasman Front that is larger than observed. This northward flow occurs because isopycnal outcropping in the ACC reduces the transport that passes south of New Zealand. Although the model seems to overestimate this effect on eastward transport south of New Zealand, isopycnal outcropping does contribute to the correct direction of the EAUC.

Including bottom topography in the 1/8° model produces meanders in the eastern portion of the Tasman Front with phases that agree well with observations. Bottom steering of the surface currents compensates for the effect on meander wavelength of the decrease in baroclinic instabilities, resulting in meanders with similar wavelengths to the flat-bottom simulation. This simulation reproduces all observed eddies north and east of New Zealand. It also reproduces all examined currents.

Increasing the resolution of the simulation to 1/16° increases the surface variability and the amount of energy generated in each layer. The geographical collocation of peaks in surface and abyssal EKE coupled with increased energy with increased resolution suggests that instabilities are responsible for the downward transport of energy. Calculations of beta Rossby numbers and analysis of dQ/dy latitude–time plots show that the instabilities are most probably mixed barotropic–baroclinic. The increased variability increases abyssal currents and, therefore, the upper-ocean–topographic coupling, resulting in larger meanders in the Tasman Front. These meanders agree well with observed wavelengths, phases, and amplitudes, but the ECE has merged with an observed low in the mean and the northward transport through the Tasman Sea is increased. Preliminary results from a 1/32° resolution model qualitatively agree with the 1/16° model, suggesting that the simulations have achieved a convergent solution. The separation of the ECC just north of the Chatham Rise seems at first glance to be a result of bottom steering, since it follows the eastward extension of bottom topography. In fact, the separation of ECC is due to the wind stress curl field.

The vertical resolution of the model results in poor agreement with observed transports in the vicinity of the ACC since all five layers outcrop, severely restricting the flow south of Australia and New Zealand. This disagreement affects the direction of the flow through the Tasman Sea and the magnitude of the EAUC and Tasman Front, resulting in larger than observed SSH variability north of New Zealand, complicating the analysis north of New Zealand and increasing the uncertainty of the conclusions. An increase in vertical resolution by the addition of more layers to the model would mitigate this effect.

Acknowledgments. This work is a contribution to the 6.1 Project "Thermodynamic and Topographic Forcing in Global Ocean Models" sponsored by the Office of Naval Research under program element 601153N. The computations in this paper were performed on AHPCRC, ARSC, CEWES, and NAVO Cray T3Es using grants of computer time from the Defense Department High Performance Computing Modernization Office. The 1/16° global simulation was performed under the FY97 DoD HPC Challenge project "1/16° Global Ocean Model" on the CEWES T3E and using early access on the NAVO T3E. The 1/32° simulation was started using early access time provided by Cray on a 1536 processor Cray T3E and completed under an FY98-00 DoD HPC Challenge project "Global and Basin-Scale Ocean Modeling and Prediction" on the NAVO T3E. CET received financial support for this work from the Department of Defense through a National Defense Science and Engineering Graduate Fellowship. The ONR Physical Oceanography Program provides a Secretary of the Navy Grant to JJO as the base support for the Center for Ocean–Atmospheric Prediction Studies (COAPS). We would like to thank Alan Wallcraft and Joseph Metzger for their model development work and computational assistance, Gregg Jacobs for supplying the TOPEX/Poseidon-derived sea surface height variability, and Dean Roemmich for supplying the observed climatological dynamic sea surface height data. We would also like to thank the reviewers for their helpful comments and suggestions on this manuscript.

APPENDIX

Explanation of Symbols and Notations

$$\nabla \cdot \mathbf{F} = \frac{1}{a\cos\theta}\frac{\partial F_\phi}{\partial \phi} + \frac{1}{a\cos\theta}\frac{\partial (F_\theta \cos\theta)}{\partial \theta}$$

$$\nabla^2\Phi = \frac{1}{a^2\cos^2\theta}\frac{\partial^2\Phi}{\partial\phi^2} \quad \frac{1}{a^2\cos\theta}\frac{\partial}{\partial\theta}\left(\frac{\partial\Phi}{\partial\theta}\cos\theta\right)$$

A = coefficient of isopycnal eddy viscosity
a = radius of the earth (6371 km)
C_b = coefficient of bottom friction
C_t = coefficient of interfacial friction
C_M = coefficient of additional interfacial friction associated with entrainment

$D(\phi, \theta)$ = total depth of the ocean at rest
$\mathbf{e}_k$ = angular deformation tensor

$$e_{\phi\phi_k} = \frac{\partial}{\partial\phi}\left(\frac{u_k}{\cos\theta}\right) - \cos\theta\frac{\partial}{\partial\theta}\left(\frac{v_k}{\cos\theta}\right) = -e_{\theta\theta_k}$$

$$e_{\phi\theta_k} = \frac{\partial}{\partial\phi}\left(\frac{v_k}{\cos\theta}\right) + \cos\theta\frac{\partial}{\partial\theta}\left(\frac{u_k}{\cos\theta}\right) = e_{\theta\phi_k}$$

$G_{kj} = g \qquad j \geq k$
$G_{kj} = g - g(\rho_k - \rho_j)/\rho_o \qquad j < k$
g = acceleration due to gravity
H_k = kth layer thickness at rest
h_k = kth layer thickness
h_k^+ = kth layer thickness at which entrainment starts
h_k^- = kth layer thickness at which detrainment starts

$$H_n = D(\phi, \theta) - \sum_{j=1}^{n-1} H_j$$

ϕ = longitude
ρ_o = constant reference density
ρ_k = kth layer density, constant in space and time
τ = wind stress

$$\tau_k = \begin{cases} \tau_w & \text{for } k = 0 \\ C_k\rho_o|\mathbf{v}_k - \mathbf{v}_{k+1}|(\mathbf{v}_k - \mathbf{v}_{k+1}) & \\ & \text{for } k = 1 \ldots n-1 \\ C_b\rho_o|\mathbf{v}_n|\mathbf{v}_n & \text{for } k = n \end{cases}$$

t = time
θ = latitude
$\mathbf{v}_k$ = kth layer velocity = $\mathbf{e}_\phi u_k + \mathbf{e}_\theta v_k$
$\mathbf{V}_k$ = $h_k\mathbf{v}_k = \mathbf{e}_\phi U_k + \mathbf{e}_\theta V_k$

$$\omega_k = \begin{cases} 0 & \text{for } k = 0, n \\ \omega_k^+ - \omega_k^- - W_k\hat{\omega}_k & \text{for } k = 1 \ldots n- \end{cases}$$

$\omega_k^+ = \tilde{\omega}_k[\max(0, h_k^+ - h_k)/h_k^+]^2$
$\omega_k^- = \tilde{\omega}_k[\max(0, h_k - h_k^-)/h_k^+]^2$
$\hat{\omega}_k = (\omega_k^+ - \omega_k^-)/\overline{W}_k$
$\tilde{\omega}_k$ = kth interface reference diapycnal mixing velocity
$W_k(\phi, \theta)$ = kth interface weighting factor for global diapycnal mixing designed to conserve mass within a layer in compensation for explicit diapycnal mixing due to $h_k < h_k^+$ (i.e., $\omega_k^+ - \omega_k^-$), and net transport through the lateral boundaries of layer k
$\overline{X(\phi, \theta)}$ = regionwide area average of X

A hydrodynamic reduced-gravity model with n active layers has the lowest layer infinitely deep and at rest, that is, $\mathbf{v}_{n+1} = 0$, $h_{n+1} = \infty$, and $\nabla h_{n+1} = 0$. The model equations for the active layers are identical to those for n-layer hydrodynamic finite-depth model, except that

$G_{kl} = g(\rho_{n+1} - \rho_k)/\rho_o \qquad l \leq k,$
$G_{kl} = g(\rho_{n+1} - \rho_l)/\rho_o \qquad l > k,$
H_n = constant,
$\tau_k = \tau_w \qquad k = 0,$
$\tau_k = C_k\rho_o|\mathbf{v}_k - \mathbf{v}_{k+1}|(\mathbf{v}_k - \mathbf{v}_{k+1}) \qquad k = 1 \quad n,$
$\omega_k = 0 \qquad k = 0,$
$\omega_k = \max(0, \omega_k^+) - \max(0, \omega_k^-) - h_k\hat{\omega}_k \qquad k = \quad n.$

REFERENCES

Andrews, J. C., M. W. Lawrence, and C. S. Nilsson, 1980: Observations of the Tasman Front. *J. Phys. Oceanogr.*, **10,** 1854–1869.

Bryan, K., and M. D. Cox, 1968: A nonlinear model of an ocean driven by wind and differential heating: Part I. Description of three-dimensional velocity and density fields. *J. Atmos. Sci.*, **25,** 945–967.

Bye, J. A. T., R. A. Heath, and T. W. Sag, 1979: A numerical model of the oceanic circulation around New Zealand. *J. Phys. Oceanogr.*, **9,** 892–899.

Campos, E. J. D., and D. B. Olson, 1991: Stationary Rossby waves in western boundary current extensions. *J. Phys. Oceanogr.*, **21,** 1202–1224.

Chiswell, S. M., 1996: Variability in the Southland Current, New Zealand. *N. Z. J. Mar. Freshwater Res.*, **30,** 1–17.

——, J. Toole, and J. Church, 1997: Transports across the Tasman Sea from WOCE repeat sections: The East Australian Current 1990–94. *N. Z. J. Mar. Freshwater Res.*, **31,** 469–475.

Da Silveira, I. C. A., G. R. Flierl, and W. S. Brown, 1999: Dynamics of separating western boundary currents. *J. Phys. Oceanogr.*, **29,** 119–144.

Davis, R. E., 1998: Preliminary results from directly measuring mid-depth circulation in the tropical and South Pacific. *J. Geophys. Res.*, **103,** 24 619–24 639.

Denham, R. N., and F. J. Crook, 1976: The Tasman Front. *N. Z. J. Mar. Freshwater Res.*, **10,** 15–30.

De Szoeke, R. A., 1987: On the wind-driven circulation of the South Pacific Ocean. *J. Phys. Oceanogr.*, **17,** 613–630.

Godfrey, J. S., 1973: Comparison of the East Australian Current with the western boundary flow in Bryan and Cox's (1968) numerical model ocean. *Deep-Sea Res.*, **20,** 1059–1076.

——, 1989: A Sverdrup model of the depth-integrated flow for the world ocean allowing for island circulations. *Geophys. Astrophys. Fluid Dyn.*, **45,** 89–112.

——, 1996: The effect of the Indonesian throughflow on ocean circulation and heat exchange with the atmosphere: A review. *J. Geophys. Res.*, **101,** 12 217–12 237.

——, G. R. Creswell, T. J. Golding, A. F. Pearce, and R. Boyd, 1980: The separation of the East Australian Current. *J. Phys. Oceanogr.*, **10,** 430–440.

Haidvogel, D. B., and W. R. Holland, 1978: The stability of ocean currents in eddy-resolving general circulation models. *J. Phys. Oceanogr.*, **8,** 393–413.

Haltiner, G. J., and F. L. Martin, 1957: *Dynamical and Physical Meteorology.* McGraw-Hill, 470 pp.

Heath, R. A., 1985a: A review of the physical oceanography of the seas around New Zealand—1982. *N. Z. J. Mar. Freshwater Res.*, **19,** 79–124.

——, 1985b: Large-scale influence of the New Zealand seafloor topography on western boundary currents of the South Pacific Ocean. *Aust. J. Mar. Freshwater Res.*, **36,** 1–14.

Heburn, G. W., 1994: The dynamics of the seasonal variability of the western Mediterranean circulation. *Seasonal and Interannual Variability of the Western Mediterranean Sea,* Vol. 46, *Coastal*

Estuarine Studies, P. E. LaViolette, Ed., Amer. Geophys. Union, 249–285.

Hellerman, S., and M. Rosenstein, 1983: Normal monthly wind stress over the world ocean with error estimates. *J. Phys. Oceanogr.,* **13,** 1093–1104.

Hogan, P. J., and H. E. Hurlburt, 2000: Impact of upper ocean–topographic coupling and isopycnal outcropping in Japan/East Sea models with 1/8° to 1/64° resolution. *J. Phys. Oceanogr.,* **30,** 2535–2561.

Holland, W. R., 1978: The role of mesoscale eddies in the general circulation of the ocean—Numerical experiments using a wind-driven quasi-geostropic model. *J. Phys. Oceanogr.,* **8,** 363–392.

——, and L. B. Lin, 1975: On the generation of mesoscale eddies and their contribution to the oceanic general circulation. I. A preliminary numerical experiment. *J. Phys. Oceanogr.,* **5,** 642–657.

Hurlburt, H. E., and J. D. Thompson, 1980: A numerical study of Loop Current intrusions and eddy-shedding. *J. Phys. Oceanogr.,* **10,** 1611–1651.

——, and ——, 1982: The dynamics of the Loop Current and shed eddies in a numerical model of the Gulf of Mexico. *Hydrodynamics of Semi-Enclosed Seas,* J. C. J. Nihoul, Ed., Elsevier, 243–297.

——, and ——, 1984: Preliminary results from a numerical study of the New England Seamount Chain influence on the Gulf Stream. *Predictability of Fluid Motions,* G. Holloway and B. J. West, Eds., American Institute of Physics, 489–504.

——, and E. J. Metzger, 1998: Bifurcation of the Kuroshio Extension at the Shatsky Rise. *J. Geophys. Res.,* **103,** 7549–7566.

——, and P. J. Hogan, 2000: Impact of 1/8° to 1/64° resolution on Gulf Stream model-data comparisons in basin-scale subtropical Atlantic Ocean models. *Dyn. Atmos. Oceans,* **32,** 283–329.

——, A. J. Wallcraft, W. J. Schmitz Jr., P. J. Hogan, and E. J. Metzger, 1996: Dynamics of the Kuroshio/Oyashio current system using eddy-resolving models of the North Pacific Ocean. *J. Geophys. Res.,* **101,** 941–976.

Huyer, A., R. L. Smith, P. J. Stabeno, J. A. Church, and N. J. White, 1988: Currents off south-eastern Australia: Results from the Australian Coastal Experiment. *Aust. J. Mar. Freshwater Res.,* **39,** 245–288.

Laing, A. K., B. R. Stanton, and P. G. Challenor, 1996: Variations in the East Auckland Current from satellite radar altimeter data. *N. Z. J. Mar. Freshwater Res.,* **30,** 175–191.

Levitus, S., 1982: *Climatological Atlas of the World Ocean.* NOAA Professional Paper 13, 173 pp.

Lilley, F. E. M., J. H. Filloux, N. L. Bindoff, and I. J. Ferguson, 1986: Barotropic flow of a warm-core ring from seafloor electric measurements. *J. Geophys. Res.,* **91,** 12 979–12 984 and 13 109.

Luyten, J. R., J. Pedlosky, and H. Stommel, 1983: The ventilated thermocline. *J. Phys. Oceanogr.,* **13,** 293–309.

McWilliams, J. C., and R. C. Flierl, 1979: On the evolution of isolated nonlinear vortices. *J. Phys. Oceanogr.,* **9,** 1155–1182.

Mesinger, F., and A. Arakawa, 1976: *Numerical Methods Used in Atmospheric Models.* GARP Publication Series, Vol. 17, World Meteorological Organization, 64 pp.

Metzger, E. J., and H. E. Hurlburt, 1996: Coupled dynamics of the South China Sea, the Sulu Sea and the Pacific Ocean. *J. Geophys. Res.,* **101,** 12 331–12 352.

——, ——, J. C. Kindle, Z. Sirkes, and J. Pringle, 1992: Hindcasting of wind-driven anomalies using a reduced-gravity global ocean model. *Mar. Technol. Soc. J.,* **26,** 23–32.

Mitchell, J. L., W. J. Teague, G. A. Jacobs, and H. E. Hurlburt, 1996: Kuroshio Extension dynamics from satellite altimetry and a model simulation. *J. Geophys. Res.,* **101,** 1045–1058.

Mitchum, G. T., 1995: The source of 90-day oscillations at Wake Island. *J. Geophys. Res.,* **100,** 2459–2475.

Moore, D. R., and A. J. Wallcraft, 1998: Formulation of the NRL Layered Ocean Model in spherical coordinates. Stennis Space Center Naval Research Laboratory Tech. Rep. NRL CR 7323-96-0005, 24 pp.

Morey, S. L., J. F. Shriver, and J. J. O'Brien, 1999: The effects of Halmahera on the Indonesian Throughflow. *J. Geophys. Res.,* **104,** 23 281–23 296.

Mulhearn, P. J., 1987: The Tasman Front: A study using satellite infrared imagery. *J. Phys. Oceanogr.,* **17,** 1148–1155.

Munk, W. H., 1950: On the wind-driven ocean circulation. *J. Meteor.,* **7,** 79–93.

Murphy, S. J., H. E. Hurlburt, and J. J. O'Brien, 1999: The connectivity of eddy variability in the Caribbean Sea, the Gulf of Mexico, and the Atlantic Ocean. *J. Geophys. Res.,* **104,** 1431–1453.

National Oceanic and Atmospheric Administration, 1986: ETOP05 digital relief of the surface of the earth. National Geophysical Data Center Data Announcement 86-MGG-07.

Ou, H. W., and W. P. M. De Ruijter, 1986: Separation of an inertial boundary current from a curved coastline. *J. Phys. Oceanogr.,* **16,** 280–289.

Phillips, N. A., 1954: Energy transformations and meridional circulations associated with simple baroclinic waves in a two-level, quasi-geostrophic model. *Tellus,* **6,** 273–286.

Ridgway, K. R., and J. S. Godfrey, 1994: Mass and heat budgets in the East Australian Current: A direct approach. *J. Geophys. Res.,* **99,** 3231–3248.

——, and ——, 1997: Seasonal cycle of the East Australian Current. *J. Geophys. Res.,* **102,** 22 921–22 936.

Roemmich, D., and P. Sutton, 1998: The mean and variability of ocean circulation past northern New Zealand: Determining the representativeness of hydrographic climatologies. *J. Geophys. Res.,* **103,** 13 041–13 054.

Semtner, A. J., and R. M. Chervin, 1992: Ocean general circulation from a global eddy-resolving model. *J. Geophys. Res.,* **97,** 5493–5550.

Shriver, J. F., and H. E. Hurlburt, 1997: The contribution of the global thermohaline circulation to the Pacific to Indian Ocean throughflow via Indonesia. *J. Geophys. Res.,* **102,** 5491–5511.

Stanton, B. R., 1976: An oceanic frontal jet near the Norfolk Ridge northwest of New Zealand. *Deep-Sea Res.,* **23,** 821–829.

——, 1979: The Tasman Front. *N. Z. J. Mar. Freshwater Res.,* **13,** 201–214.

——, 1981: An oceanographic survey of the Tasman Front. *N. Z. J. Mar. Freshwater Res.,* **15,** 289–297.

——, P. J. H. Sutton, and S. M. Chiswell, 1997: The East Auckland Current, 1994–95. *N. Z. J. Mar. Freshwater Res.,* **31,** 537–549.

Stramma, L., R. G. Peterson, and M. Tomczak, 1995: The South Pacific Current. *J. Phys. Oceanogr.,* **25,** 77–91.

Sverdrup, H. U., 1947: Wind-driven currents in the baroclinic ocean: With application to the equatorial currents of the eastern Pacific. *Proc. Nat. Acad. Sci. U.S.A.,* **33,** 318–326.

Tilburg, C. E., 2000: Ocean dynamics around New Zealand. Ph.D. thesis, The Florida State University, Tallahassee, Florida, 106 pp. [Available from The Florida State University, Tallahassee, FL 32306.]

Uddstrom, M. J., and N. A. Oien, 1999: On the use of high-resolution satellite data to describe the spatial and temporal variability of sea surface temperatures in the New Zealand region. *J. Geophys. Res.,* **104,** 20 729–20 751.

Wallcraft, A. J., 1991: The Navy Layered Ocean Model users guide. Stennis Space Center Naval Research Laboratory NOARL Rep. 35, 21 pp.

——, and D. R. Moore, 1997: A scalable implementation of the NRL Layered Ocean Model. *Parallel Comput.,* **23,** 2227–2242.

Warren, B. A., 1970: General circulation of the South Pacific. *Scientific Exploration of the South Pacific,* Warren S. Wooster, Ed., U. S. National Academy of Science 33–49.